Master's Thesis

Enhanced air stability of $CsPbX_3$/ZnS heterostructures through selective defect healing and its organic photovoltaics application

Jinhee Cho

Department of Chemical Engineering

Graduate School of UNIST

2018

Enhanced air stability of $CsPbX_3$/ZnS heterostructures through selective defect healing and its organic photovoltaics application

Jinhee Cho

Department of Chemical Engineering

Graduate School of UNIST

Enhanced air stability of $CsPbX_3$/ZnS heterostructures through selective defect healing and its organic photovoltaics application

A thesis/dissertation
submitted to the Graduate School of UNIST
in partial fulfillment of the
requirements for the degree of
Master of Science

Jinhee Cho

12. 15. 2017

Approved by

Advisor
Jongnam Park

Enhanced air stability of $CsPbX_3$/ZnS heterostructures through selective defect healing and its organic photovoltaics application

Jinhee Cho

This certifies that the thesis/dissertation of Jinhee Cho is approved.

12. 15. 2017

signature

Advisor: Jongnam Park

signature

Jae Sung Son: Thesis Committee Member #1

signature

Kwangjin An: Thesis Committee Member #2

Abstract

Colloidal quantum dots (QDs) have been intensively studied in the past decades such as Cd-based QDs and InP QDs. Perovskite nanocrystals (NCs), which have excellent optical properties, recently have received attention as promising materials for applications in optoelectronic devices such as photovoltaics, light emitting diodes (LEDs), lasing, and bio-imaging. Perovskite NCs also exhibit excellent optical and electronic properties such as narrow emission linewidth, high photoluminescence quantum yield (PLQY), and tunability of band gap through control of composition.

Lead halide perovskites which have Pb^{2+} as a divalent cation are classified into either organic–inorganic ($CH_3NH_3^+$) or all-inorganic (Cs^+). Typically, organic-inorganic hybrid perovskites are susceptible to moisture and oxygen because they have an unstable organic cation. In contrast, all-inorganic perovskites are relatively more stable than organic-inorganic hybrid perovskites. However, there are many reports to enhance the stability of perovskite NCs such as infiltration into mesoporous materials, polymer coating and ligand replacement because all-inorganic perovskites still have stability issues. These studies have problems of escaping from mesoporous materials or interfering with carrier transport. Therefore, inorganic passivation is recently emerging as promising alternative to improve the stability of all-inorganic perovskites.

QDs are generally stabilized by enclosing shells with inorganic materials such as ZnS. In this work, $CsPbX_3$/ZnS heterostructures were synthesized by growing ZnS on $CsPbX_3$ to enhance the stability of perovskite NCs. $CsPbX_3$/ZnS heterostructures could be synthesized at room temperature by using Zn-OAm^{2+} as a Zn precursor and DDA-S^{2-} as a S precursor with good reactivity. In addition, the band gap of $CsPbX_3$/ZnS heterostructures were tunable by controlling the precursor amount and the optical and structural properties were characterized by UV-vis, PL, TRPL, XRD, TEM and ICP-OES. The synthesized $CsPbBrI_2$/ZnS exhibited improved stability over about 18 days compared to pristine $CsPbBrI_2$ which changed to the yellow phase in 2 days. Finally, organic photovoltaics with $CsPbBrI_2$/ZnS heterostructures had improved PCE and device stability compared to untreated reference cell.

Blank page

Contents

List of figures

List of tables

Chapter I. Introduction of perovskites and its stability issues

1.1 Introduction of perovskites

1.1.1 The definition of perovskites

Recently, research on nanomaterials has been carried out because of the dimension in bulk materials becomes smaller and exhibits various quantum size effects. It results in new extraordinary electronic, optical, mechanical, and chemical properties that did not exist previously. Especially, perovskite nanomaterials have been intensively investigated due to their attractive optical properties. Metal halide perovskites were first studied by Weber in the 1970s, but its properties were poor.[1] In the 1990s, Mitzi et al first made devices using perovskites materials, which has been a breakthrough in the improvement of properties since then.[2]

Metal halide perovskites have a general formula of ABX_3, where A is a monovalent cation ($CH_3NH_3^+$, $CH_3(NH_2)_2^+$, Cs^+), B is a divalent cation (Pb^{2+}, Sn^{2+}, Ge^{2+}), and X is a halide (Cl, Br, I) anion. The crystal structure of metal halide perovskites is shown in Figure 1, where the B cation is coordinated to six X halide anions in an octahedral configuration. The $[BX_6]$ octahedra are corner-sharing by a weak van der Waals force, with the A cation located in between those octahedra.[3]

In a ABX_3 perovskite structure, there is an important parameter termed as tolerance factor: $R_A + R_X = t\sqrt{2}(R_B + R_X)$, where R_A, R_B, and R_X are the ionic radii of the A, B, and X ions, respectively. To maintain the perovskite structure, the value of *t* should range from 0.8 to 1.1. In metal halide perovskites, the Cs^+ inorganic cation and the organic molecules such as methylammonium (MA^+; $CH_3NH_3^+$), formamidinium (FA^+; $CH_3(NH_2)_2^+$) are fit into the A site. Therefore, metal halide perovskites are classified into either organic-inorganic (hybrid) or all-inorganic, depending on whether the A cation is an organic molecule or an inorganic cation. Organic-inorganic perovskites exhibit excellent optical properties, but they have poor stability against moisture, oxygen and heat, accelerating the decomposition.[4,5] Therefore, research on FA or Cs based perovskites with higher durability have drawn tremendous attention, so this paper focuses on all-inorganic $CsPbX_3$ perovskite nanocrystals (NCs)..

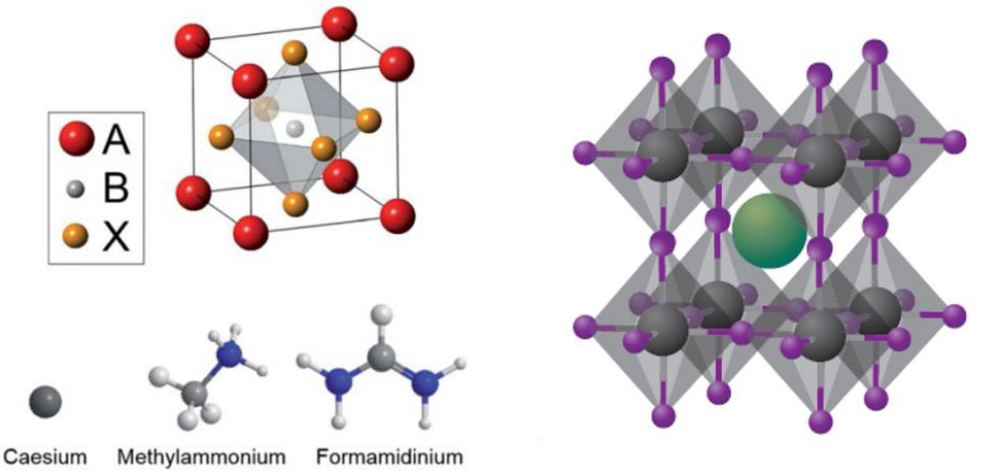

Figure 1. The crystal structure of perovskite with ABX_3 formula.[6,7]

1.1.2 Synthesis of perovskite nanocrystals

All-inorganic $CsPbX_3$ perovskite NCs can be synthesized by hot-injection method or precipitation method.

Hot-injection method is most widely used which makes the nanocrystals by swiftly injection of precursors at high temperatures. It has a good crystal structure because it reacts at high temperature and it is easy to control the particle size. Because it was reacted at high temperature, nanocrystals synthesized by hot-injection method have good crystal structure and it is easy to control size. Kovalenko et al. were first to report on cesium lead halide perovskite NCs with high PLQY by hot-injection method.[9] After dissolving PbX_2 in mixed solution with octadecene, oleylamine and oleic acid, Cs-oleate solution is then swiftly injected to mixed solution and immediately cooled by ice-bath, leading to synthesize $CsPbX_3$ NCs.

In the precipitation method, ions forming perovskites move from soluble to insoluble solvent within a few seconds at room temperature, so that nanocrystals are synthesized by supersaturated recrystallization. Metal halide perovskites have an ionic bonding characteristic that enables their facile formation at low temperatures. This method is advantageous in that it is easy to synthesize because it does not need to apply heat and be synthesized under inert atmosphere. In addition, it takes less time to experiment and it is easy for large scaled production for application. However, there are some problems that the precipitation method results in the nanocrystals with poor quality and inhomogeneity compared to the nanocrystals synthesized by the hot-injection method. It is also important to find suitable good and poor solvents for supersaturated recrystallization. Li et al. was first reported the synthesis of $CsPbX_3$ nanocrystals by precipitation method where PbX_2 and CsX were dissolved in N,N-dimethylformamide (DMF) or dimethyl sulfoxide (DMSO) and then oleylamine and oleic acid were added as ligands.[8] After then, precipitation of $CsPbX_3$ nanocrystals synthesized immediately as soon as the precursor solution was poured into toluene, which is a poor solvent, under vigorously stirring.

The perovskite nanocrystals with different wavelengths can be easily synthesized by the anion exchange method because the perovskites can be controlled the band gap by varying the halide composition. G. Nedelcu et al. introduced the anion exchange of $CsPbX_3$ NCs.[10] The halide is replaced by a vacancy-assisted diffusion mechanism, so anion-exchange could easily be performed in the cases of Cl-to-Br, Br-to-Cl, Br-to-I, and I-to-Br anion-exchanges. However, this is not achieved with Cl-to-I or I-to-Cl because the ionic radii difference between I^- and Cl^- is very large.

1.1.3 Characteristics of perovskite nanocrystals

Generally, the quantum confinement effect appears when the size of a semiconductor material becomes smaller than the Bohr radius of excitons. As the size of the material becomes smaller, the continuous energy level is changed to the discrete energy level because the space that the exciton can move becomes smaller, which changes the optical properties of absorption and emission properties. Therefore, it is possible to control the band gap by varying the size of the particles less than exciton Bohr radius. Typically, the smaller the particle size of nanomaterials, the larger the band gap, so that the nanomaterials can emit the light at shorter wavelength. The exciton Bohr radius of $CsPbX_3$ perovskite NCs is calculated to be about 7 nm, and L. Protesescu et al. investigated the quantum-size effects of the size of $CsPbBr_3$ NCs by controlling the size of 5-12 nm and identified the agreement with the theoretical values.[9]

Metal halide perovskites have attracted tremendous interest because these materials exhibit high charge carrier mobility, small exciton binding energy and long diffusion length.[11-13] Furthermore, metal halide perovskites show intriguing optical properties such as high PLQY (up to 90%), narrow emission linewidths (12-50 nm) and tunability of absorption and emission spectrum from UV to near-IR through halide composition.[14,15] Therefore, metal halide perovskites have been intensively applied for various applications such as solar cells, light-emitting diodes (LEDs), photodetector and lasing.

However, there is a stability issues by moisture, light, and temperature despite the superior optical properties of metal halide perovskites. Due to low formation energy, metal halide perovskites are easily decomposed into PbX_2 and other byproducts. Especially, organic-inorganic perovskites are more easily decomposed than all-inorganic perovskites due to the unstable organic cation. On the other hand, $CsPbX_3$ perovskites exhibit improved thermal stability due to their low melting point of 400-500 °C ($MAPBX_3$ at about 150-200 °C and $FAPbI_3$ at about 290-300 °C). Nevertheless, there is still thermodynamic instability of $CsPbX_3$ perovskites because the Cs ions are a little small to fit to the A site. $CsPbX_3$ perovskites are metastable at room temperature at first, but it is transformed into a more stable orthorhombic structure which is called yellow phase due to instability. In addition, $CsPbI_3$ perovskites can rapidly convert to orthorhombic phase because iodide-based perovskites are more unstable, but the reason for this phenomenon still remains unclear. Therefore, a number of researches have been reported to improve the stability of $CsPbX_3$ with the longer wavelength and which will be described in chapter 1.3.

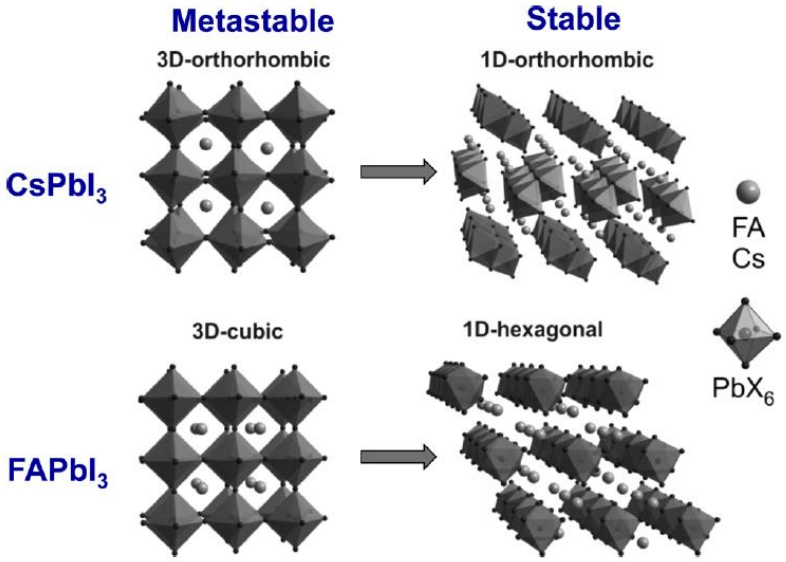

Figure 2. The illustration of crystal structure showing decomposition of $CsPbI_3$ and $FAPbI_3$.[16]

1.2 Applications with perovskites nanocrystals

Metal halide perovskites have attracted tremendous interest due to broad absorption spectrum, high charge carrier mobility, small exciton binding energy and long diffusion length. Furthermore, metal halide perovskites show intriguing optical properties such as high PLQY (up to 90%), narrow emission linewidths (12-50 nm) and tunability of absorption and emission spectrum from UV to near-IR through halide composition. Therefore, metal halide perovskites have been intensively applied for various applications such as solar cells, light-emitting diodes (LEDs), photodetector and lasing.

1.2.1 Perovskite nanocrystals in solar cells

Perovskite-based solar cells have been reported the power conversion efficiency (PCE) of 3.8% for the first time in 2009 and reached to 22.7% in 2017 by the intense research efforts, leading to impressive progress.[17,18] Metal halide perovskites were applied to dye-sensitized solar cells instead of dye molecules by Miyasaka et al in 2009 and it showed an efficiency of 3.8%. After then, perovskite solar cells have shown tremendous progress, achieving high efficiencies above 22% by intensive research in 8 years, but these high efficiencies are based on not perovskite nanocrystals but perovskites films. Although most of the reported efficient solar cell devices are based on perovskite films, there have been several recent attempts in employing perovskite NCs as active materials, too.

$CsPbI_3$ is an ideal light absorber material because it has the small band gap of about 1.73 eV compared to $CsPbCl_3$ or $CsPbBr_3$. However, $CsPbI_3$ is unstable and can convert to yellow phase under ambient condition, so that it was difficult to apply to solar cells. E. Eperon et al demonstrated perovskite solar cells with $CsPbI_3$ NCs for the first time in 2005, where solar cell devices in a variety of architectures exhibited efficiency up to 2.9% for a planar heterojunction architecture.[19] They could synthesize stabilized black perovskite phase at room temperature by careful processing control and development of a low-temperature phase transition route.

Recently, Swarnkar et al reported that the PCE based on $CsPbI_3$ NCs exhibited up to 10.77% which is the highest value with $CsPbI_3$ NCs.[20] They developed a process to purify $CsPbI_3$ NCs by using methyl acetate as an antisolvent that can isolates the $CsPbI_3$ NCs without full removal of surface species, which is critical to phase-stable photovoltaic devices. Subsequently, they fabricated $CsPbI_3$ films by spin coating of stable $CsPbI_3$ NCs for several times. The $CsPbI_3$ films also exhibited good stability when exposed into the ambient atmosphere for 60 days.

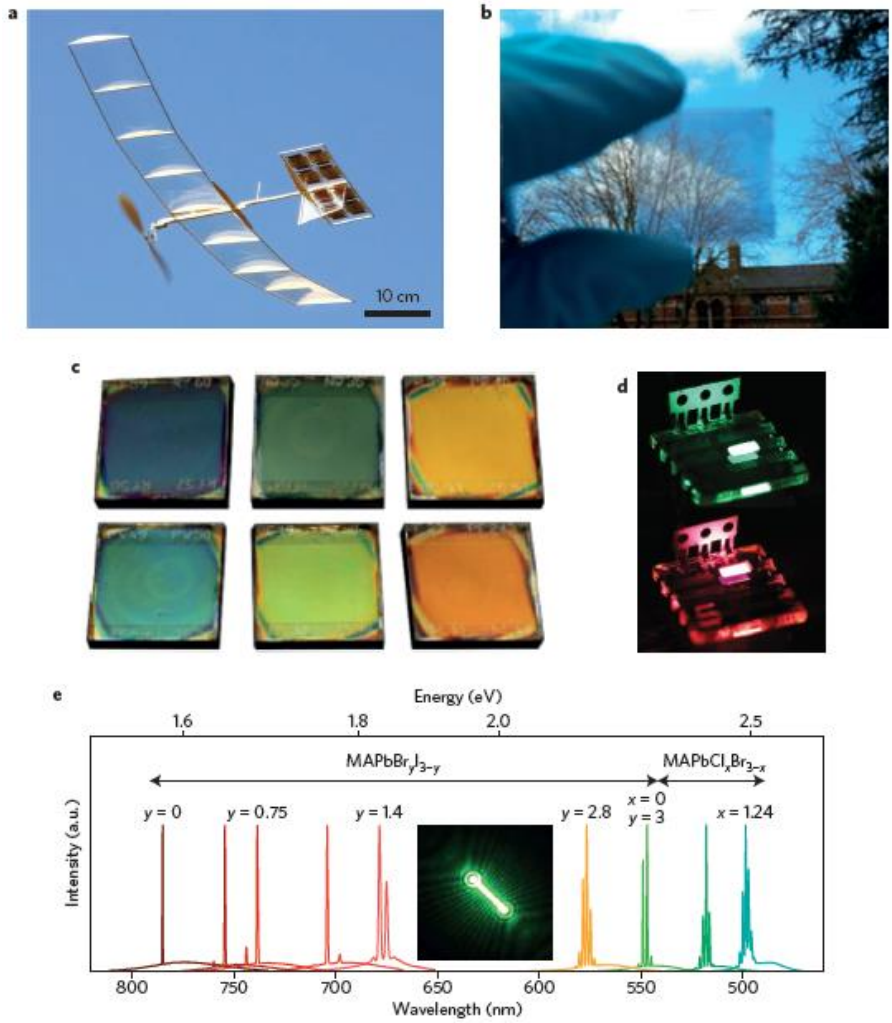

Figure 3. Various applications of metal halide perovskites. (a) a model plane powered by perovskite photovoltaics. (b) semi-transparent perovskite film. (c) colorful perovskite solar cells. (d) green and red perovskite light-emitting diodes e) tunable lasing emission wavelength.[21]

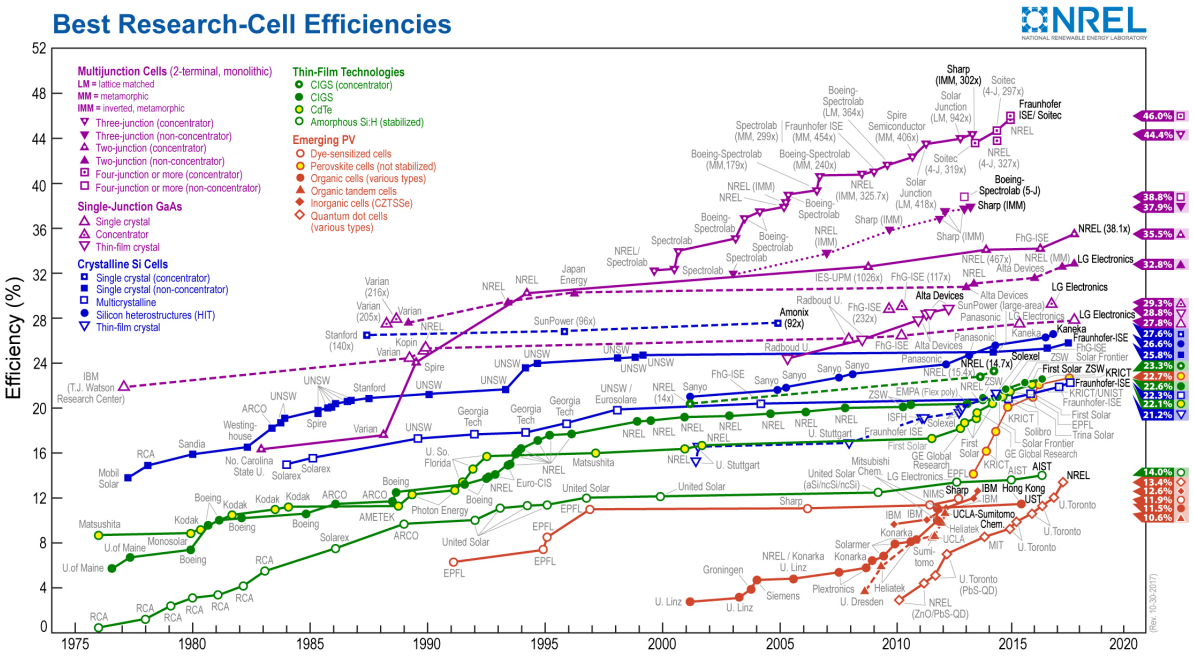

Figure 4. Best research-cell efficiencies from NREL (2017)[18]

1.2.1 Perovskite nanocrystals in light-emitting diodes (LEDs)

Metal halide perovskites are attracting attention as promising materials for LEDs due to their exceptional optical properties such as tunable emission wavelength with high PLQY, low cost and high color purity with the FWHM of 12-50 nm, which attributes to wide-color-gamut and high color-rendering index. Figure 5 shows a color gamut of $CsPbX_3$ NCs achieving up to 140% of the North American National Television Standards Committee (NTSC). For LED applications, a smaller grain size is preferred, which limits exciton diffusion. Because it increases the possibility of radiative recombination, using perovskites nanocrystals as active materials can show better performance compared to solution-prepared perovskite films.

LEDs based on $CsPbX_3$ NCs were first reported by Song et al in 2015.[22] They synthesized blue, green and orange emitting $CsPbX_3$ NCs with emission wavelengths of 455, 516 and 586 nm, respectively, and applied them to LEDs. The device was fabricated with stacking layered structure of ITO/PEDOT:PSS/PVK/QDs/TPBi/LiF/Al and achieved the luminances of 742, 964 and 528 cd/m^2 with external quantum efficiency (EQE) of 0.07, 0.12 and 0.09%. This study is significant in that $CsPbX_3$ NCs were applied to LEDs for the first time, but it was still inferior to organic-inorganic perovskites which have already been actively researched. This is because the charge transport is disturbed due to the poor configuration of LEDs and the long ligands surrounding the $CsPbX_3$ NCs.

Since then, the LEDs based on perovskite NCs have been developed rapid, the green LEDs with green-emitting $CsPbBr_3$ NCs reached EQE of about 9% and luminance of about 15,000 cm/m^2.[23] Also, the red LEDs with $CsPbI_3$ NCs showed EQE of 7.25% and luminance of 435 cd/m^2.[24] However, blue LEDs which have a low luminance of 35 cd/m^2 still remain a challenge.[25] In addition, the commercial display must be stable for at least 30,000 hours, but perovskite NCs have a problem about degradation of structures for using as an LED pixel.

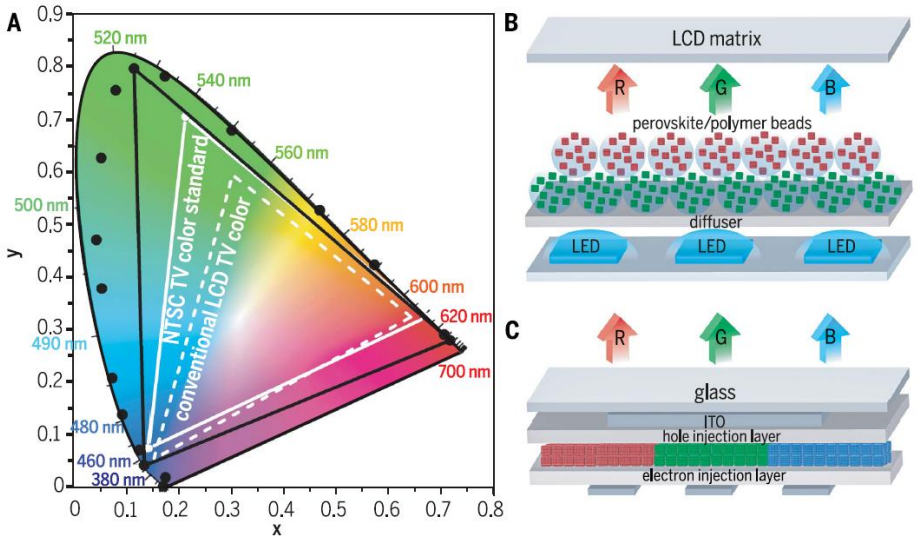

Figure 5. (a) PL spectra of $CsPbX_3$ NCs plotted on CIE chromaticity coordinates (black points) (b) Operation principle of a QD LCD display (c) Schematic of a LED pixels with LHP NCs.[26]

1.3 Synthetic strategies toward improving the stability of perovskites nanocrystals

As mentioned above, the instability of perovskite NCs is an important issue. Degradation of perovskite NCs can happen due to several external factors, such as moisture, oxygen, high temperature and UV light. Indeed, many researcher have reported the various approaches to improve the stability of perovskite NCs.

1.3.1 Infiltration of perovskite nanocrystals into mesoporous materials

One of the methods to increase the stability of perovskite NCs is infiltration of perovskite NCs into mesoporous materials such as SiO_2, TiO_2, and Al_2O_3. The use of mesoporous templates has the advantages which are inexpensive, easy to synthesis, and the original properties are well maintained by the intrinsic tolerance to the defects.[27,28]

However, this method cannot completely prevent the perovskite NCs from being exposed to ambient air, although mesoporous materials can stabilize the perovskite NCs. Furthermore, there are some several problems that perovskite NCs can partially escape from the pores and cannot be completely separated from other materials.

Dirin et al reported the stabilized perovskite NCs entrapped within mesoporous silica (meso-SiO_2) matrixes, showing stability with the pore size and bright PL with quantum efficiencies exceeding 50%.[29] They investigated the optical properties of entrapped $CsPbX_3$ and other perovskites according to pore size of meso-SiO_2, so that the case of 7 nm-SiO_2 showed slower PL decay rates and improved stability because of similar particle size of perovskite NCs.

JY Sun et al reported a two-step synthesis method for perovskite NCs embedding in zeolite-Y with increased stability under ambient atmosphere compared to bare $CsPbX_3$.[30] The thermal stability of the $CsPbBr_3$-Y composites was confirmed by the change of emission intensity according to the temperature, and the emission intensity reached half of the initial intensity at 100 °C, which is higher than bare $CsPbBr_3$ NCs (60 °C). Additionally, the blue-shift of the emission was smaller for $CsPb(Br_{0.5}I_{0.5})_3$-zeolite-Y composites (23 nm over 13 days) than bare NCs (28 nm over 6 days) due to enhanced stability by infiltration into mesoporous zeolite. They also fabricated a White-LEDs (WLEDs) by combining a blue InGaN LED chip with $CsPbBr_3$-zeolite-Y composites and $CsPb(Br_{0.4}I_{0.6})_3$ NCs.

1.3.2 Polymer coating on perovskite nanocrystal

Polymer coating or encapsulation of perovskite NCs are also other effective ways to enhance the stability of perovskite NCs. The dense polymer matrices can especially enhance the resistance for water

and acid. Despite these advantages, however, polymer coating has been regarded as a suitable method for applying to films or bulk materials, and studies applied to perovskite nanoparticles have not yet been studied extensively. In addition, organic materials surrounding the surface of nanocrystals can interfere with charge transport, which is a disadvantage for optoelectronic or catalytic applications.

Yi Wei et al demonstrated the enhanced stability of perovskite NCs by encapsulation in crosslinked polystyrene beads toward superior water resistance.[31] They synthesized the highly luminescent $CsPbBr_3$@Polystyrene composite beads via simple swelling-shrinking strategy, retaining the strong luminescence after being immersed into water over nine months. Moreover, the composites exhibited the improved stability in harsh environments such as acid/alkali aqueous solution, so that they carried out the LEDs and cellular labeling agents using $CsPbBr_3$@PS composites.

Meyns et al used the poly(maleic anhydride-alt-1-octadecene) (PMA) into the synthesis of the perovskite NCs for increasing about UV irradiation stability.[32] The PMA as the ligand shell stabilized the perovskite NCs by tightening the ligand bingding and limiting the interaction of NCs with the surrounding media. When the $CsPbBr_3$-PMA NCs was under continuous illumination by a 365 nm pump in ambient conditions, the emission intensity maintained with 60% of peak area remaining after 12 hours, compared to $CsPbBr_3$ NCs with no PMA protection, decreasing down to 21%. Therefore, they further showed the application for WLEDs with $CsPbBr_3$-PMA NCs embedded in silicone/glass plates.

1.3.3 Ligand replacement of perovskite nanocrystals

Generally, perovskite NCs are capped with long chain such as oleylamine and oleic acid, and these ligands are repeatedly attached and detached in the form of oleylammonium halides and oleylammonium oleates on the them. The ligands prevent the perovskite NCs from aggregation and helps to remain stable NCs, but excess ligands from the NCs solution promote a phase transformation. Also, too short ligands make perovskite NCs unstable in solution, and too long ligands interfere with charge transport like the polymer coating method described above. Therefore, it is difficult to select the appropriate ligand to satisfy various factors.

Chujie W et al reported the stabilized $CsPbI_3$ NCs by using alkyl phosphinic acid as a replacement for conventionally used oleic acid.[33] Here, CS-TMPPA for using as Cs precursor can be synthesized in ODE at room temperature by using bis-(2,2,4-trimethylpentyl)phosphinic acid (TMPPA), while the OA-based precursor such as Cs–oleate requires heating up to 100 °C before dissolution occurs. The absorption spectra of $CsPbI_3$–OA show a progressively larger scattering over only 3 days, with yellow precipitates forming in that period and he PL intensity simultaneously declined. In contrast, the absorption and PL properties of $CsPbI_3$–TMPPA are almost perfectly preserved after 20 days of storage under ambient conditions.

Jun Pan et al demonstrated ultra-air and photostable $CsPbBr_3$ quantum dots (QDs) by using an inorganic−organic hybrid ion pair as the capping ligand.[34] They used didodecyl dimethylammonium bromide (DDAB) was used as a source of DDA^+ to passivate the perovskite $CsPbBr_3$ NCs and induced ultrastable amplified spontaneous emission (ASE) not only through one photon but also through two-photon absorption processes. The untreated sample suffered from partial degradation within hours, showing a sharp contrast in performance, whereas the passivated perovskite film exhibited the same threshold and optical characteristics even after 4 months of open air storage and rounds of photostability testing, providing clear evidence of the ultrastability of perovskite coated films under ambient conditions.

1.3.4 Inorganic passivation of perovskite nanocrystals

The above-mentioned methods have several disadvantages that perovskite NCs can escape from pores of mesoporous materials, and organic molecules for polymer coating and ligand replacement can interfere with charge transport for optoelectronic application. Furthermore, considering intrinsically dynamic interactions between organic ligands and surfaces of $CsPbX_3$ NCs, immobilized inorganic passivation could work better than organic passivation for effective stabilization of $CsPbX_3$ NCs. Therefore, many researchers are recently interested in inorganic passivation in order to improve the stability of perovskite NCs, but inorganic passivation of perovskite NCs is still a challenge.

Woo JY et al proposed stable $CsPbBr_3$ NCs passivated by metal halide such as $ZnBr_2$ with high PLQY, showing enhanced stability over 6 days.[35] As a result, nearly 60% of original PL QY was retained for the case of $ZnBr_2$-$CsPbBr_3$ NCs compared to about 20% retained in the case of pristine-$CsPbBr_3$ NCs in ambient condition with very high relative humidity (RH) up to 60%. Inorganic Zn cation is not likely to contribute to enhancement of PLQY and its stability, highlighting the importance of inorganic surface passivation of $CsPbX_3$ NCs.

Chapter II. Synthesis and characterization of $CsPbX_3$/ZnS heterostructure and its organic photovoltaics application

2.1 Introduction

Metal halide perovskites have attracted tremendous interest as promising materials because of their outstanding optical and electronic properties. Metal halide perovskites show high PLQY (up to 90%), narrow emission linewidths (12-50 nm) and tunability of absorption and emission spectrum from UV to near-IR through halide composition. However, there is a stability issue by moisture, light, and temperature despite the superior properties of metal halide perovskites. Due to low formation energy, metal halide perovskites are easily decomposed into PbX_2 and other byproducts.

In order to increase the stability of semiconductor nanomaterials, it has been studied about the form of core-shell or heterostructure. Hines et al. reported the encapsulating inorganic materials on semiconductor NCs for the first time, and then most of the NCs improved their optical properties and stability with a core-shell structure.[36] However, perovskite NCs with the core-shell structure have not yet been reported since perovskite have an ionic bonding characteristic different from other semiconductor materials.

Recently, Chen et al reported $CsPbX_3$/ZnS heterostructures with enhanced stability and high crystalline quality for the first time.[37] The stability of red-emitting $CsPbBr_{3-x}I_X$/ZnS heterostructures were identified through the change of PL spectra. The PL spectra of $CsPbBr_{3-x}I_X$/ZnS heterostructures could keep for about 12 days without any protection in air. In contrast, the PL spectra of pure $CsPbBr_{3-x}I_x$ NCs blue-shifted within 1 day in the same condition, indicating that the stability was improved by formation of heterostructure with inorganic materials. They also demonstrated $CsPbX_3$/ZnS heterostructures by systematic density functional theory based first-principle calculations. Photoluminescence measurement results show a decrease of recombination lifetime with increasing reaction time, so that they suggest $CsPbX_3$/ZnS heterostructures are beneficial in photovoltaic applications. However, there are some problems that purification after synthesis is not perfect, and reproduction is not performed well.

Therefore, it is necessary to develop new synthetic method that is effective and easy to form $CsPbX_3$/ZnS heterostructures. In this work, I developed a facile method to synthesize $CsPbX_3$/ZnS heterostructures at room temperature by using precursors of ligand type with high reactivity. I choose OAm-Zn^{2+} as a Zn precursor and DDA-S^{2-} as a S precursor, and these precursors were injected into purified perovskite NCs solution under inert conditions at room temperature to form $CsPbX_3$/ZnS heterostructures. The synthesis procedure of DDA-S^{2-} is followed the previous report by Jiang P et al.[38] The synthesized red-emitting $CsPbBrI_2$/ZnS heterostructures showed improved stability by blue-

shifting of emission peaks only about 50 nm over 18 days compared to pristine $CsPbBrI_2$. In addition, when $CsPbBrI_2$/ZnS heterostructures were applied to organic photovoltaics, they showed improved efficiency and stability over 8 days.

2.2 Experimental session

2.2.1 Materials

Cesium carbonate (99.9%), Lead bromide, 98%, Lead(II) iodide(99%), oleylamine (OAm, 98+%), oleic acid (OAc, 90%), 1-octadecene (ODE, technical grade, 90%), zinc acetate (99.99%), Didecyldimethylammonium bromide (DDAB, 98%), Sodium sulfide were purchased from Sigma-Aldrich. Benzene (99.5%), Acetonitrile (99.5%) was purchased from SAMCHUN. All chemicals above were used directly without any purification.

2.2.2 Synthesis of Cs-oleate solution

0.163 g of cesium carbonate, 0.5 mL of OAc and 8 mL of ODE were added to a 50 mL three-neck round-bottomed flask. This solution was degassed for 1 h at 120 °C. After purged with argon, the temperature was heated up to 150 °C under argon flow until the cesium carbonate was completely dissolved.

2.2.3 Synthesis of $CsPbBr_3$ NCs

First, 69 mg of lead bromide was dissolved in 5 mL of ODE in a 50 mL three-neck round-bottomed flask. This solution was degassed for 1 h at 120 °C and then filled with Ar. Then, 0.5 mL of OAm, 0.5 mL of OAc were added to the reaction flask. After complete solubilization of a PbX_2 salt, the mixture was heated to 160 °C for 10 min. After 20 min, 0.4 mL of Cs-oleate solution was injected swiftly into the reaction flask under vigorous stirring and react for 5 sec. The solution was then cooled to room temperature by using ice-bath.

The crude solution was subsequently centrifuged at 7830 rpm for 10 min. The supernatant was discarded and the precipitates were redispersed in benzene. For further purification, acetonitrile was added and the mixture was centrifuged at 7830 rpm for 5 min. Finally, the precipitate was redispersed in benzene.

2.2.4 Synthesis of $CsPbBrI_2$ NCs

First, 23 mg of lead bromide and 57.8 mg of lead iodide was dissolved in 5 mL of ODE in a 50 mL three-neck round-bottomed flask. This solution was degassed for 1 h at 120 °C and then filled with Ar.

Then, 0.7 mL of OAm, 0.7 mL of OAc were added to the reaction flask. After complete solubilization of a PbX_2 salt, the mixture was heated to 150 °C for 10 min. After 20 min, 0.4 mL of Cs-oleate solution was injected swiftly into the reaction flask under vigorous stirring and react for 5 sec. The solution was then cooled to room temperature by using ice-bath.

The crude solution was subsequently centrifuged at 7830 rpm for 10 min. The supernatant was discarded and the precipitates were redispersed in benzene. For further purification, acetonitrile was added and the mixture was centrifuged at 7830 rpm for 3 min. Finally, the precipitate was redispersed in benzene.

2.2.5 Preparation of Zn and S precursors

To prepare OAm-Zn^{2+} as Zn precursor, 27.5 mg of zinc acetate was dissolved in 1 mL of OA m and 2 mL of toluene.

For the preparation of DDA-S^{2-} as S precursor, 61 mg of DDAB was dissolved in 3 mL of toluene. After that, the S^{2-} anions were transferred from water to toluene phase through mixing toluene containing DDAB and 0.05 M aqueous Na_2S solution. The toluene phase was separated and used as sulfur precursor (DDA-S^{2-}).

2.2.6 Synthesis of $CsPbX_3$/ZnS heterostructures

For the synthesis of $CsPbX_3$/ZnS heterostructures, 1 mL of 15 mg/ml $CsPbX_3$ solution was added to a 50 mL three-neck round-bottomed flask under inert conditions. Zn and S precursors was injected slowly into the reaction flask under vigorous stirring. After 30 min from the injection, the mixture was purified by washing them with 0.3 mL of acetonitrile and subsequently centrifuging. Then, the precipitates were redispersed in benzene.

2.2.7 Characterization methods

Absorption spectra were recorded using a UV-Vis spectrophotometer obtained from Shimadzu UV-1800. Photoluminescence (PL) spectra were collected using an Agilent FL 1004 M008. Measurements for nanocrystal solutions were performed for each sample at room temperature. Time-resolved PL (TRPL) measurements were performed with a time-correlated single-photon counting setup (FluoTime 300, PicoQuant) at room temperature. The samples were excited by a 510 nm CW and pulsed diode laser head (LDH-D-C 450 and LDH-D-C 510) coupled with a laser diode driver (PDL 820, PicoQuant)

and a repetition rate of between 196 kHz and 40 MHz. The peak photon count was set to 10000 for all measurements. The PL lifetime (τ) was obtained by fitting the decay curve with an exponential decay function. TEM images were obtained using a JEOL JEM-2100 microscope (200 kV). The TEM samples were prepared by depositing the perovskite solutions on copper grids. XRD patterns were collected using a Rigaku Ultimate-IV X-ray diffractometer operated at 40 kV/200 mA using the Cu Kα line (λ=1.5418 A) and the scan rate was 1 degree/min. XRD samples were prepared by placing the perovskite powder samples on glass substrates. ICP-OES characterization was carried out with a Varian 700-ES equipped with 40 MHz free running RF generator.

2.3 Result & Discussion

2.3.1 A new route to synthesis of $CsPbX_3$/ZnS heterostructures

Perovskite NCs were typically synthesized for a very short time of 5 seconds. On the other hand, Zn and S precursors such as zinc stearate and dodecanethiol used in ZnS synthesis must react at high temperature for a long time. If Zn and S precursors are added at high temperature and react for a long time after the perovskite synthesis, the growth of perovskite NCs may continue. There is also a difficulty in the process of purifying excess Zn and S precursors remaining after the reaction.

In this work, I propose a facile strategy to synthesize $CsPbX_3$ NCs adsorbed with ZnS and find that the synthesized $CsPbX_3$/ZnS heterostructures has high quality with enhanced stability. I choose OAm-Zn^{2+} as a Zn precursor and DDA-S^{2-} as a S precursor because it has high reactivity at room temperature. The synthesis procedure of $CsPbX_3$ is followed the previous report by Protesescu et al.[9] After perovskite NCs synthesis and washing, OAm-Zn^{2+} and DDA-S^{2-} precursors are injected into perovskite NCs solution under inert conditions at room temperature to form $CsPbX_3$/ZnS heterostructures.

To investigate the effect of Zn and S precursors, optical and structural analysis was performed on samples that Zn and S precursors injected simultaneously and respectively. There was no significant difference in the absorption and PL spectra for the samples added Zn and S precursors respectively and simultaneously (Figure 6a,b). In addition, XRD and TEM analysis were carried out to confirm the structure and morphology of $CsPbBr_3$/ZnS. The XRD patterns of $CsPbBr_3$ NCs, with only OAm-Zn^{2+}, with only DDA-S^{2-} and with OAm-Zn^{2+} and DDA-S^{2-} are shown in Figure 6c,d. For $CsPbBr_3$ NCs, the XRD pattern is the same as a cubic $CsPbBr_3$ phase without other peaks. $CsPbBr_3$ with only OAm-Zn^{2+} and DDA-S^{2-} respectively also shows only the cubic phase. For $CsPbBr_3$/ZnS NCs, however, additional diffraction peaks of ZnS can be observed at ≈28° in addition to the XRD peaks of cubic $CsPbBr_3$ phase, indicating the formation of ZnS heterostructure. These additional peaks can be indexed as the hexagonal ZnS (JCPDS No. 10-0434).

As shown in figure 7, it can be clearly seen that $CsPbBr_3$ NCs have cubic shape with an average size of ≈17 nm. Furthermore, sphere shaped dots of 5 nm with different phases were observed when Zn and S precursors were added at the same time, which is in agreement with the XRD data. The interplanar distance of 0.56 nm for $CsPbBr_3$ NCs is well consistent with the (001) plane of cubic-phase $CsPbBr_3$ NCs. Moreover, the inset in figure is the HR-TEM image of ZnS with the interplanar distance of 0.33 nm which are consistent with the (002) plane of ZnS (Figure 7d). It means that ZnS was successfully synthesized on $CsPbBr_3$ NCs, forming heterostructure.

In addition to optimize the reaction conditions, I identified various reaction parameters for $CsPbX_3$/ZnS heterostructures such as reaction temperature, time, precursors amount. First, the synthesis

was carried out by raising the reaction temperature, but the decomposition of $CsPbBr_3$ NCs, which the $CsPbBr_3$ NCs turned into a yellow phase, occurred when the reaction temperature was increased to more than 80 °C. When the $CsPbX_3$/ZnS heterostructures reacted at more stable 50 °C than 80 °C, the $CsPbX_3$/ZnS heterostructures were aggregated and it can be observed through scattering in the absorption spectrum. However, no significant change was observed in the PL data (Figure 8). TEM images also show that $CsPbX_3$/ZnS heterostructures are aggregated and there are ZnS dots with the size of about 4 nm inside and outside of the $CsPbBr_3$ NCs (Figure 9).

In addition to the reaction temperature, I was explored the absorption and PL spectra of $CsPbBrI_2$/ZnS heterostructures with the amount of precursors. As shown in Figure 10a,b, the first excitonic peak in absorption spectrum and PL peak were gradually blue-shifted as the amount of Zn and S precursors increase. In literature, there are many reports on blue-shift of PL spectra when ZnS shell enclose the semiconductor core.[39,40] As the contents of ZnS increase, the reason for the blue-shift is that the energy gap of ZnS is larger than that of $CsPbBr_3$ or $CsPbI_3$, which causes charge transfer. However, when the reaction time was decreased or increased, there was almost no change in the first excitonic peak and the PL peak (Figure 10c,d). Therefore, the band gap is not affected by the reaction time but influenced by the amount of precursors in this synthesis method due to formation of ZnS.

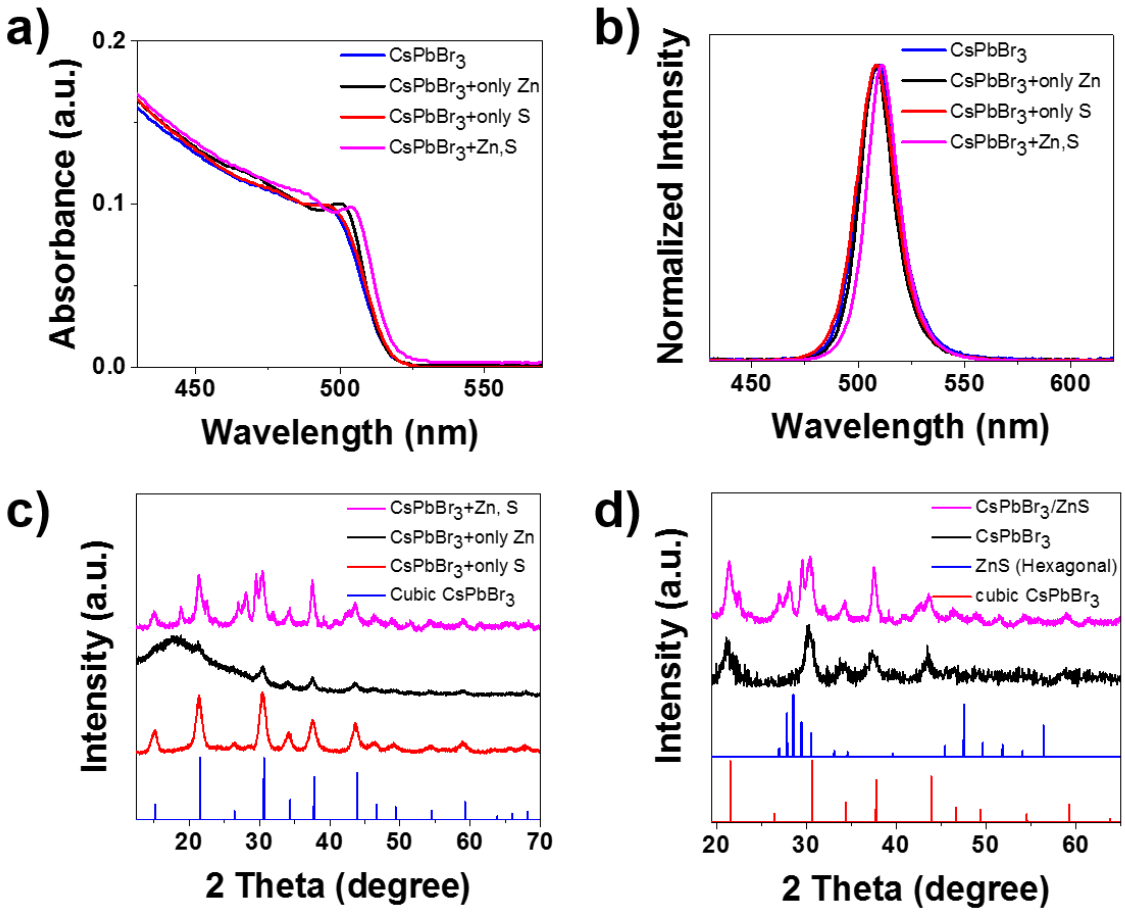

Figure 6. (a) UV-vis absorption spectra, (b) PL emission spectra, (c) XRD patterns of $CsPbBr_3$ with respective precursors, (d) XRD patterns of $CsPbBr_3$/ZnS heterostructures.

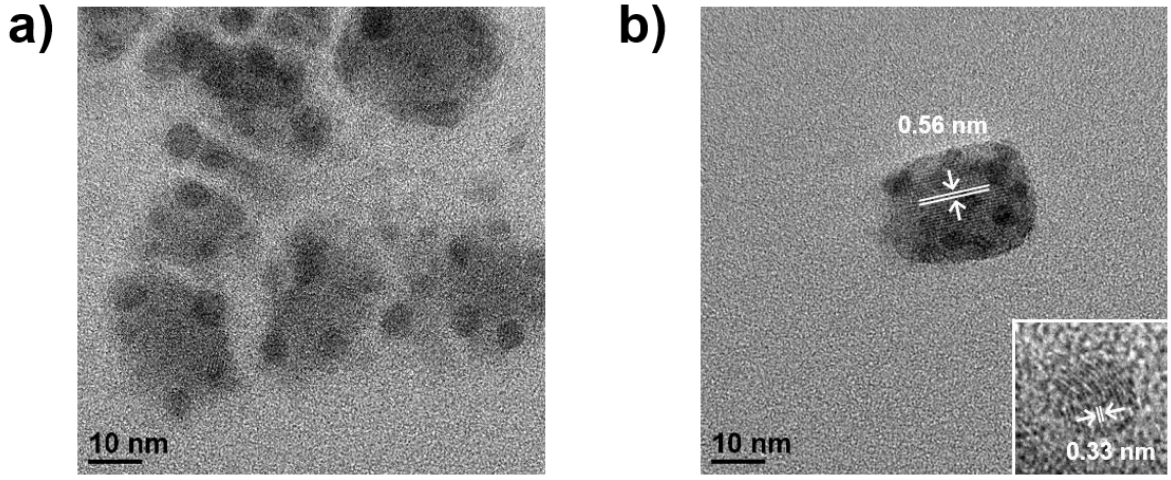

Figure 7. (a) Low-magnification TEM image (250K), (b) HR-TEM image of $CsPbBr_3$/ZnS heterostructures.

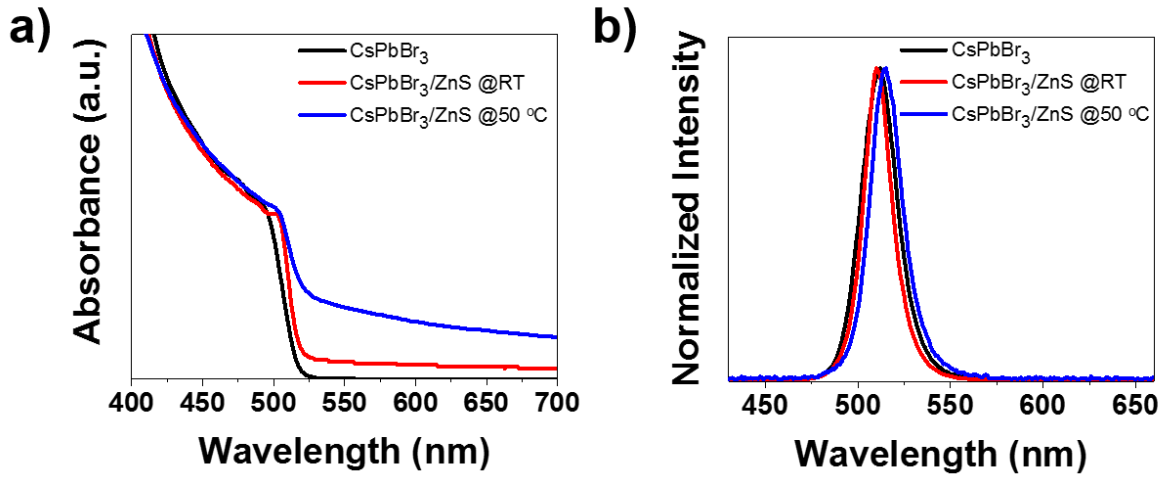

Figure 8. (a) UV-vis absorption spectra, (b) PL emission spectra of $CsPbBr_3$/ZnS heterostructures reacted at various temperatures

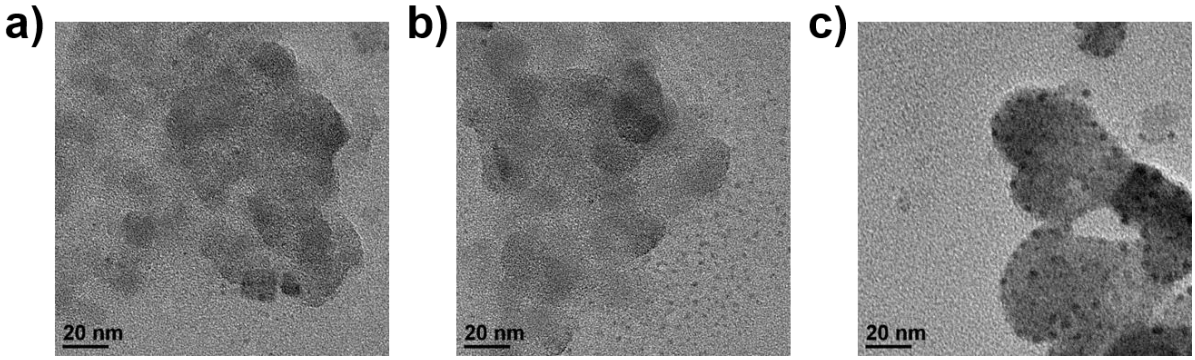

Figure 9. TEM images of $CsPbBr_3$/ZnS heterostructures reacted at various temperatures.

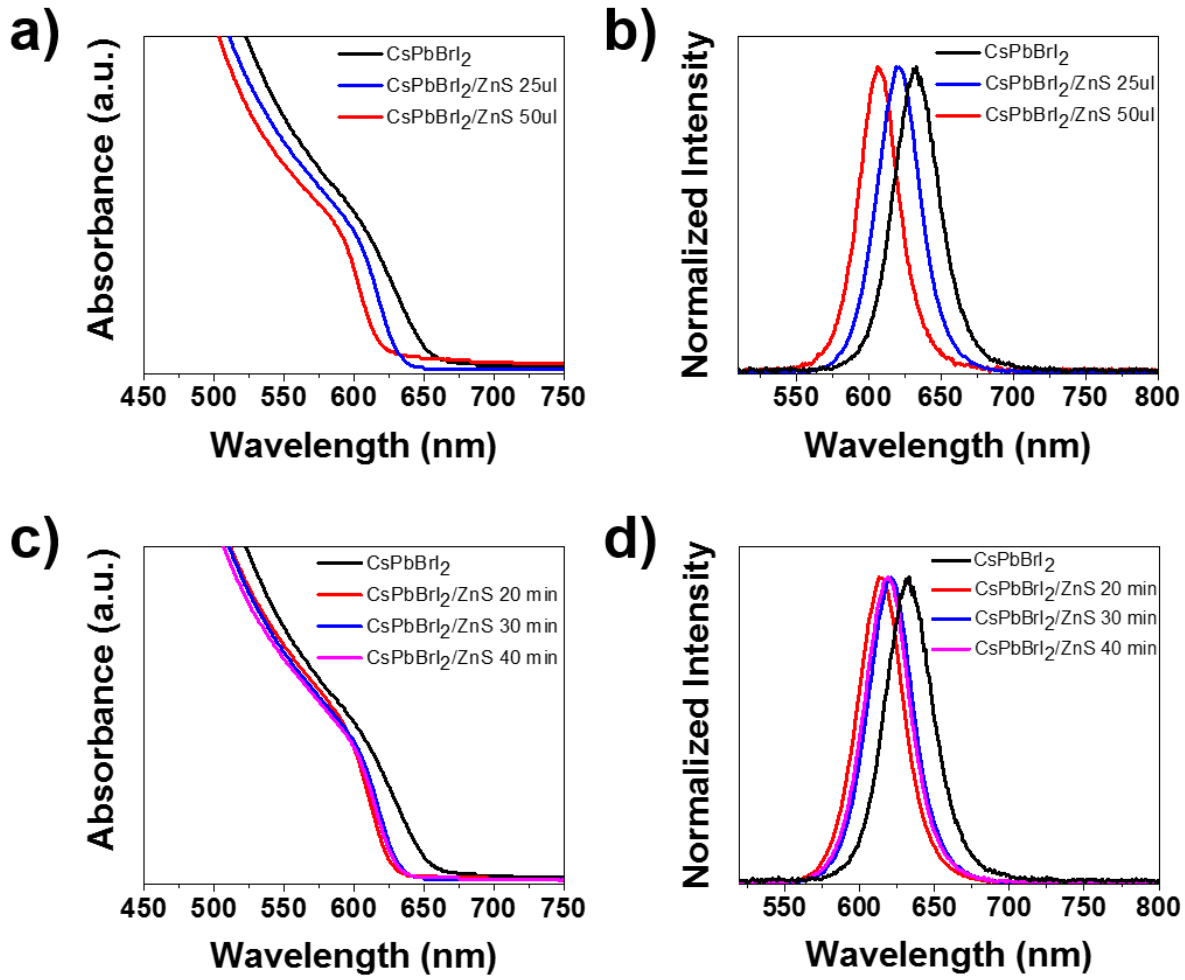

Figure 10. (a) UV-vis absorption spectra, (b) PL emission spectra of $CsPbBr_3$/ZnS heterostructures with the amount of precursors, (c) UV-vis absorption spectra, (d) PL emission spectra of $CsPbBr_3$/ZnS heterostructures with the time.

2.3.2 Study about synthesis process

To identify the synthesis mechanism, I investigated how the $CsPbX_3$/ZnS heterostructures are synthesized and the important factors in synthesis process. First, Zn and S precursors were injected through the washing process after synthesis of $CsPbBr_3$ NCs in the above synthesis process, but I tried to synthesize $CsPbBr_3$/ZnS heterostructures by injecting Zn and S precursors without washing process to investigate the effect of the washing step. After the synthesis of $CsPbBr_3$ NCs, $CsPbBr_3$/ZnS heterostructures was not formed when Zn and S precursors were injected in the crude solution after the quenching to room temperature without washing. It can be seen that the crystallinity is weakened by the broadening of the first excitonic peak in the absorption spectrum and the PL peak is slightly red-shifted (Figure 11a,b). Since XRD analysis can most accurately identify the structure of the material, the structure of the products reacted in the crude solution was analyzed by XRD. As a result of XRD analysis, XRD pattern shows no additional peak in addition to cubic $CsPbBr_3$ or change of the existing peak, indicating that structural changes did not occur (Figure 11c). This is because Zn and S precursors are prevented from reacting to each other due to excess reactants that were initially put in. Therefore, it can be seen that the $CsPbBr_3$/ZnS heterostructures were formed only after washing through these results, so that it seems that the reaction occurs when Zn and S precursors meet at the defect site after washing process.

In order to demonstrate that the reaction to form ZnS takes place at the defect site, the formation of $CsPbBr_3$/ZnS heterostructures were confirmed when the defect was removed through the ligand washing which adds the ligands during washing process. For the ligand washing, oleylamine and oleic acid as ligands were respectively added in a volume of 50 μl per batch. Increasing PL intensities indicates that the addition of ligands reduces the defect and improves the optical properties (Figure 12a,b). However, the color of the solution turned into white after about 5 minutes when Zn and S precursors were added to $CsPbBr_3$ NCs solution after ligand washing to form $CsPbBr_3$/ZnS heterostructures (Figure 12c). As a result of analyzing the solution turned white color, a strong absorption peak was generated at about 330 nm, which is an absorption peak of ZnS nanoparticles.[41] In the TEM image, some $CsPbBr_3$ NCs were present, but most of particles consisted of ZnS dots in the form of spheres with the size of about 5 nm (Figure 12d). In addition, ZnS peak was observed through XRD pattern, indicating that the newly formed materials are ZnS nanoparticles, and the peaks of $CsPbBr_3$ NCs which pre-existed mostly disappeared (Figure 12e).

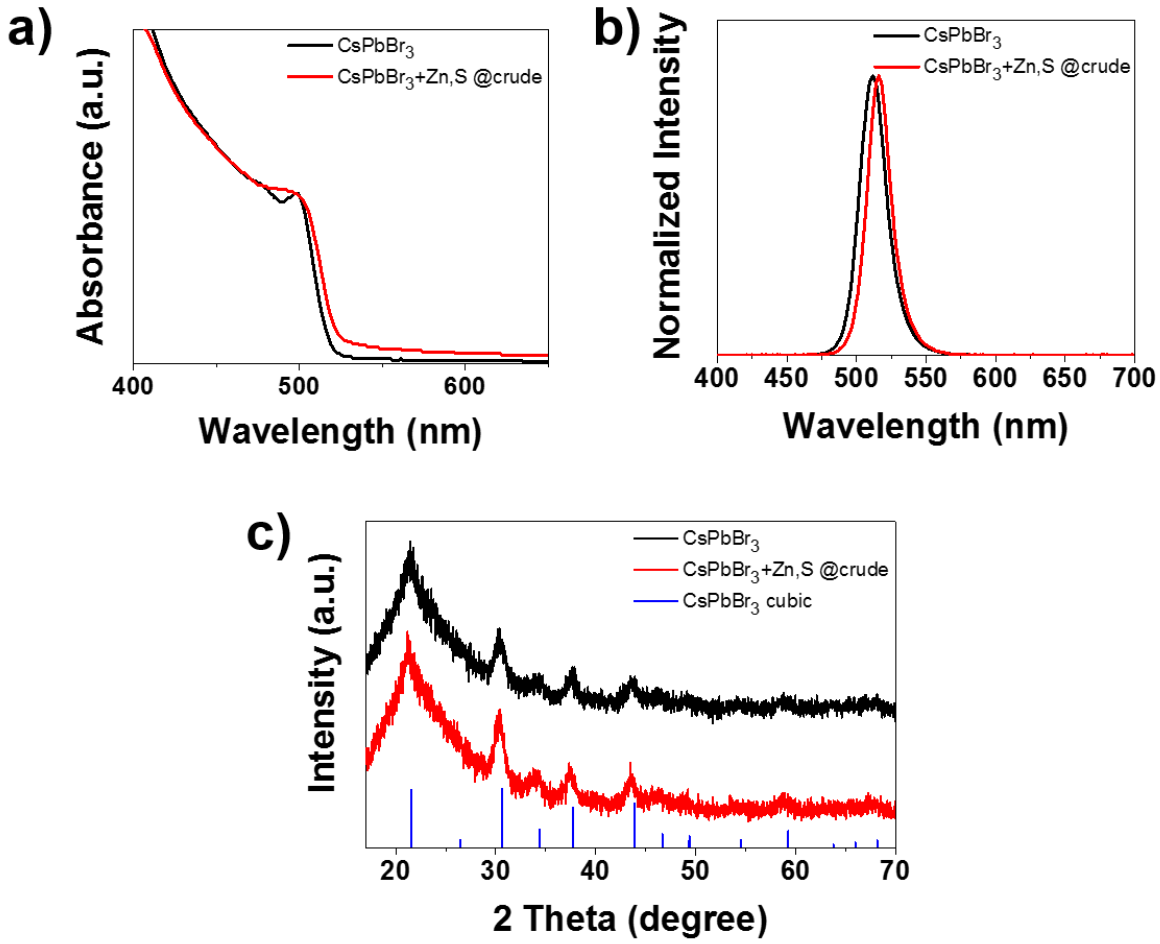

Figure 11. (a) UV-vis absorption spectra, (b) PL emission spectra, c) XRD patterns of $CsPbBr_3$/ZnS heterostructures when Zn and S precursors were injected in the crude solution.

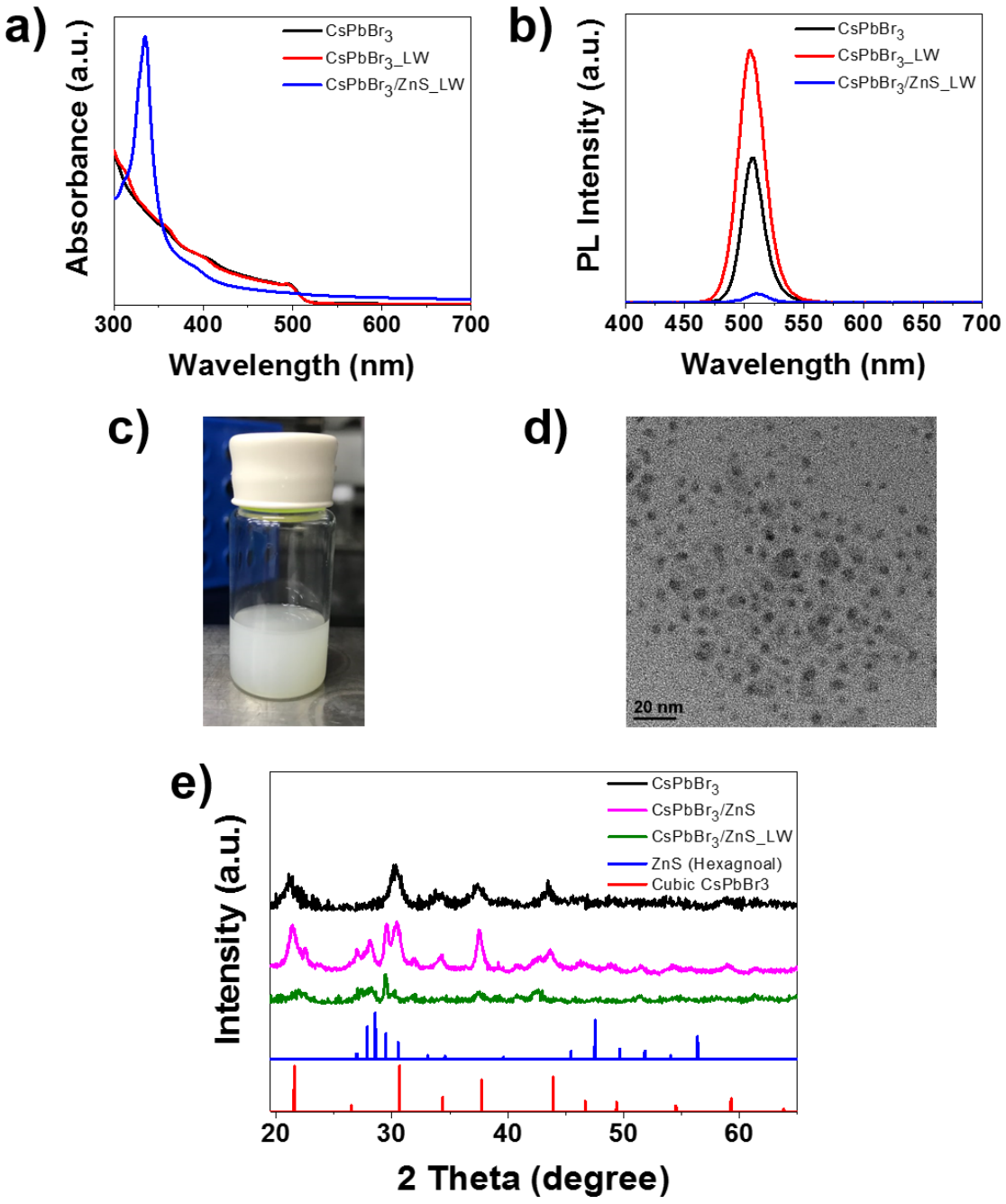

Figure 12. (a) UV-vis absorption spectra, (b) PL emission spectra, (c) photograph image, (d) TEM image (e) XRD patterns of $CsPbBr_3$/ZnS heterostructures synthesized after ligand washing,

2.3.3 Characterization of $CsPbX_3$/ZnS heterostructures

Previously, $CsPbBr_3$/ZnS heterostructures have been characterized for distinct structural analysis, but synthesis and characterization of red-emitting $CsPbBrI_2$/ZnS heterostructures based on $CsPbBrI_2$ NCs are essential for solar cell application. Similar to the previous method, $CsPbBrI_2$/ZnS heterostructures were synthesized by adding same amount of Zn and S precursors to the $CsPbBrI_2$ NCs solution simultaneously. Compared to $CsPbBr_3$/ZnS heterostructures, if the excessive amount of Zn and S precursors were added to the $CsPbBrI_2$ NCs solution, $CsPbBrI_2$ NCs were turned into ZnS nanoparticles, so that each precursor were added in an appropriate amount with 50 μl or less. Various characterizations were performed about $CsPbBrI_2$, $CsPbBrI_2$/ZnS_10 and $CsPbBrI_2$/ZnS_20, which were added 10 and 20 μl of precursors into the $CsPbBrI_2$ NCs, respectively.

First, PL emission peak of $CsPbBrI_2$ shows at 625.4 nm with FWHM of 35.8 nm and the PLQY is 30%. PL emission peaks were also observed at 623.0 nm for $CsPbBrI_2$/ZnS_10 and 617.3 nm for $CsPbBrI_2$/ZnS_20. As the amount of Zn and S precursors increased, the first excitonic peak in absorption spectrum and the PL emission peak tended to shift slightly to shorter wavelength, which already mentioned the effect of the precursor amount (Figure 13). The PLQY was changed from 30 to 45 or 61% by increasing the amount of Zn and S precursors, respectively, but FWHM was almost similar for all cases (Table 1). Here, the increase of PLQY is due to the reduction of defects, as shown in chapter 2.3.2.

To understand the decay dynamics of $CsPbBrI_2$/ZnS heterostructures, I studied the time-resolved PL (TRPL) decay spectra with different precursors amount (Figure 14). The obtained PL decay spectra were fitted by a second order exponential model. In the table 2, τ_1 and τ_2 mean non-radiative and radiative recombination lifetime, respectively, and A_1 and A_2 indicate the respective amplitude constant ratios. For $CsPbBrI_2$, non-radiative recombination lifetime is 96.4 ns and contributes 20.8% to the whole emission profile. Also, the radiative recombination lifetime is 23.1 ns and contributes 79.2%. As the amount of Zn and S precursors were increased, the contribution of non-radiative recombination increased and that of radiative recombination decreased, but both non-radiative and recombination lifetime decreased, leading that the average lifetime decreased. Particularly, the decrease of recombination lifetime affects the charge diffusion length and makes the photovoltaic performance improve.[small]

TEM analysis was carried out to investigate the morphology and size. In the case of $CsPbBrI_2$, the edge length was about 10 nm. In $CsPbBrI_2$/ZnS_10, however, the edge length was increased to 15 nm and the ZnS with sphere shape was slightly observed (Figure 15). Also, ZnS dots were more observed in $CsPbBrI_2$/ZnS_20 which added more Zn and S precursors. In the HR-TEM image, the interplanar distance of $CsPbBrI_2$ NCs was 0.56 nm and the that of ZnS was 0.33 nm respectively, which was

consistent with the literature value. Unfortunately, the peaks for all the elements were observed in the EDS spectrum, but the sensitivity was so low that the values of atomic percent were not obtained (Figure 16). Therefore, ICP-OES analysis precisely measured the ratio of elements, but only results of element analysis for Pb, Zn, and S are obtained since there was a limitation that Cs, Br, and I elements could not be measured by ICP-OES. Pb:Zn was 100:1.1 in $CsPbBrI_2$/ZnS_10 and 100:1.6 in $CsPbBrI_2$/ZnS_20, where there was a small proportion of zinc because the amount of added Zn and S precursors was very small. Also, the ratio of Zn to S was 1.1:4.2 for $CsPbBrI_2$/ZnS_10 and 1.6:4.8 for $CsPbBrI_2$/ZnS_20, which S existed about 3 to 3.8 times higher than Zn (Table 3-5).

As a result of XRD analysis for additional structural analysis, ZnS peak was additionally observed at about 28° after the addition of Zn and S precursors to $CsPbBrI_2$ (Figure 17). However, the intensity of the XRD patterns were low and it was difficult to distinguish peaks clearly because the amount of added Zn and S precursors was small and the positions of $CsPbBrI_2$ and ZnS peaks are similar.

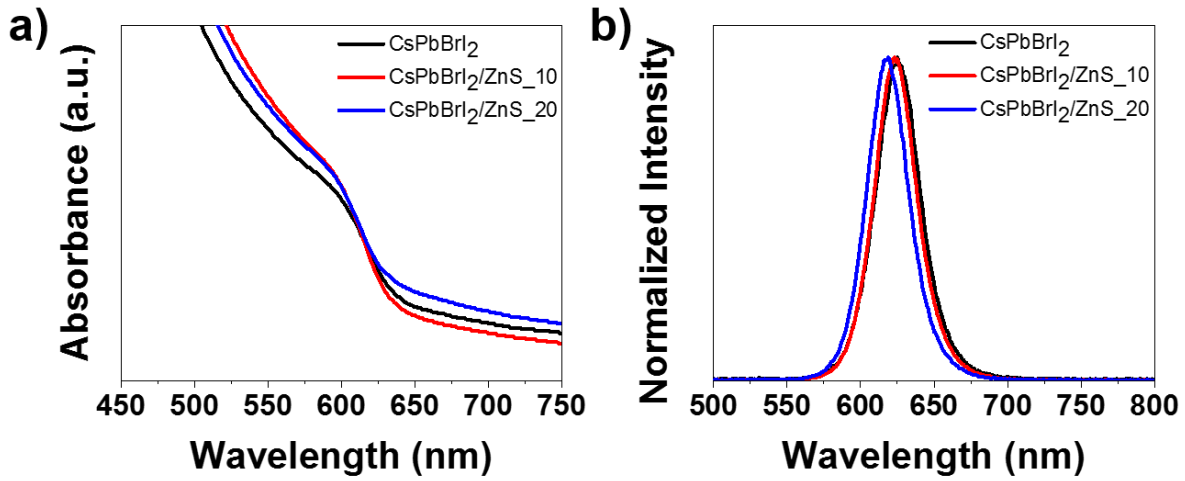

Figure 13. (a) UV-vis absorption spectra, (b) PL emission spectra of $CsPbBrI_2$/ZnS heterostructures with the amount of precursors.

Table 1. Emission wavelength, FWHM and quantum yield of $CsPbBrI_2$/ZnS heterostructures.

	Emission wavelength (nm)	**FWHM (nm)**	**Quantum yield (%)**
$CsPbBrI_2$	625.4	35.8	30
$CsPbBrI_2$/ZnS_10	623.0	36.0	45
$CsPbBrI_2$/ZnS_20	617.3	35.9	61

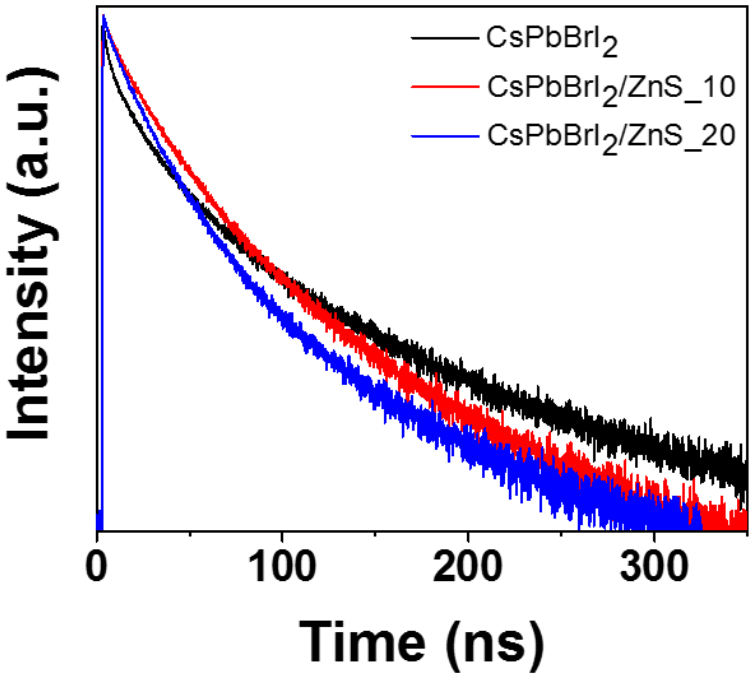

Figure 14. PL decay curves of $CsPbBrI_2$/ZnS heterostructures with the precursor amount fitted by exponential model.

Table 2. PL decay time components and amplitudes of the exponential fit curves.

	A_1 (%)	τ_1 (ns)	A_2 (%)	τ_2 (ns)	τ_{avg} (ns)
$CsPbBrI_2$	20.8	96.4	79.2	23.1	38.3
$CsPbBrI_2$/ZnS_10	21.8	67.1	78.2	22.2	31.9
$CsPbBrI_2$/ZnS_20	34.2	54.7	65.8	18.3	30.7

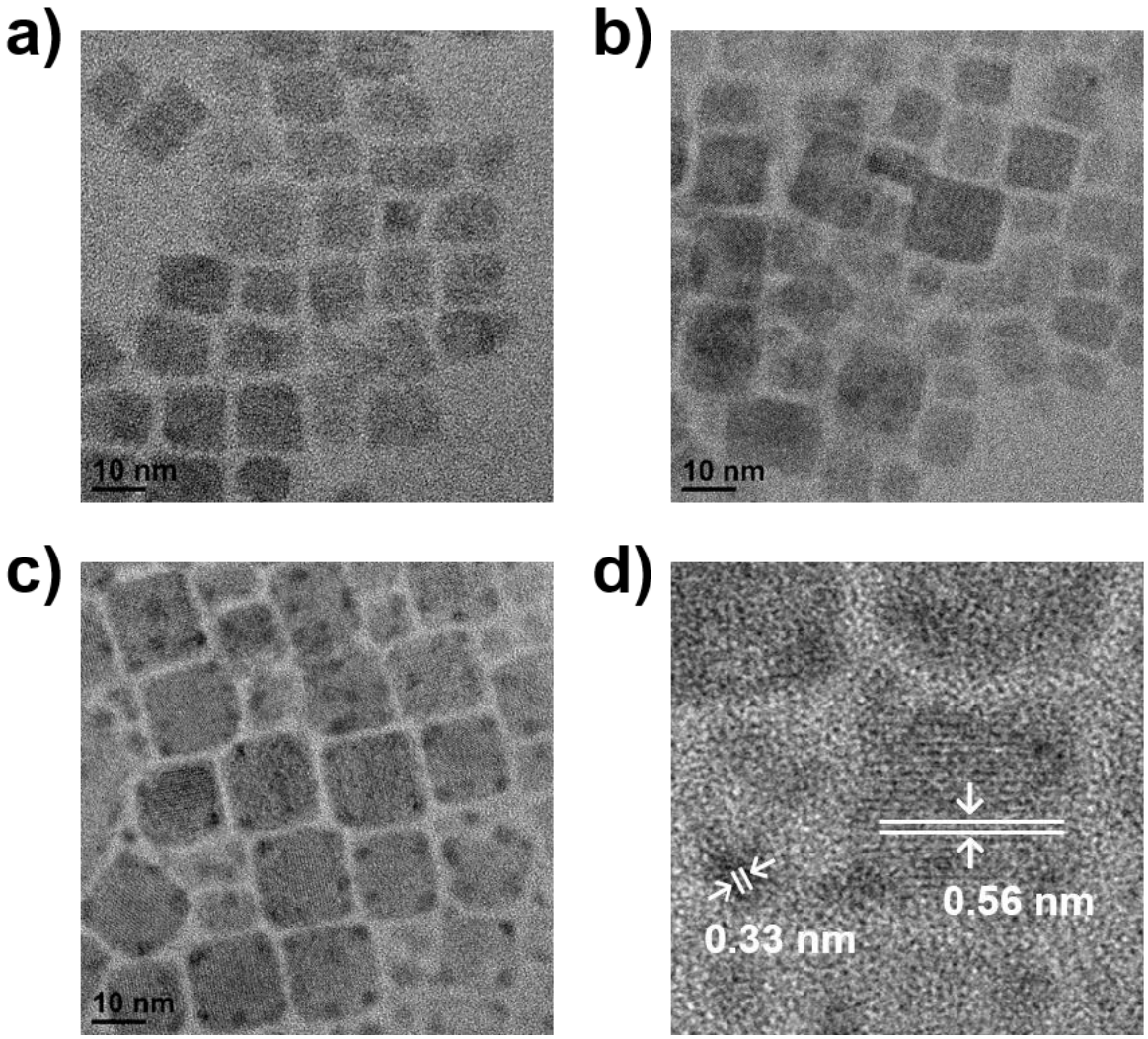

Figure 15. TEM images of (a) pristine $CsPbBrI_2$ NCs, (b) $CsPbBrI_2$/ZnS_10, (c) $CsPbBrI_2$/ZnS_20, (d) HR-TEM image of $CsPbBrI_2$/ZnS_20.

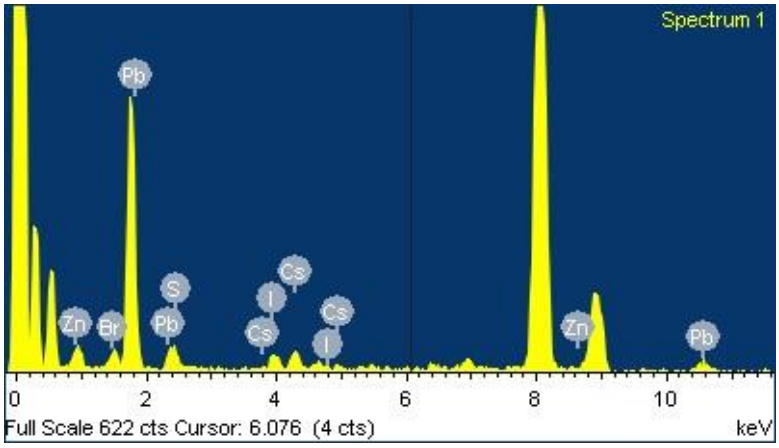

Figure 16. EDS spectra of $CsPbBrI_2$/ZnS_20.

Table 3 ICP-OES data of pristine $CsPbBrI_2$ NCs.

Element	Conc (mg/kg)	Conc (mmol/kg)	ratio
Pb	8.41	0.03817	

Table 4. ICP-OES data of pristine $CsPbBrI_2$/ZnS_10.

Element	Conc (mg/kg)	Conc (mmol/kg)	ratio
Pb	6.56	0.02977	100
Zn	0.071	0.000332	1.1
S	0.229	0.001258	4.2

Table 5. ICP-OES data of pristine $CsPbBrI_2$/ZnS_20.

Element	Conc (mg/kg)	Conc (mmol/kg)	ratio
Pb	8.41	0.026911	100
Zn	0.092	0.00043	1.6
S	0.235	0.00129	4.8

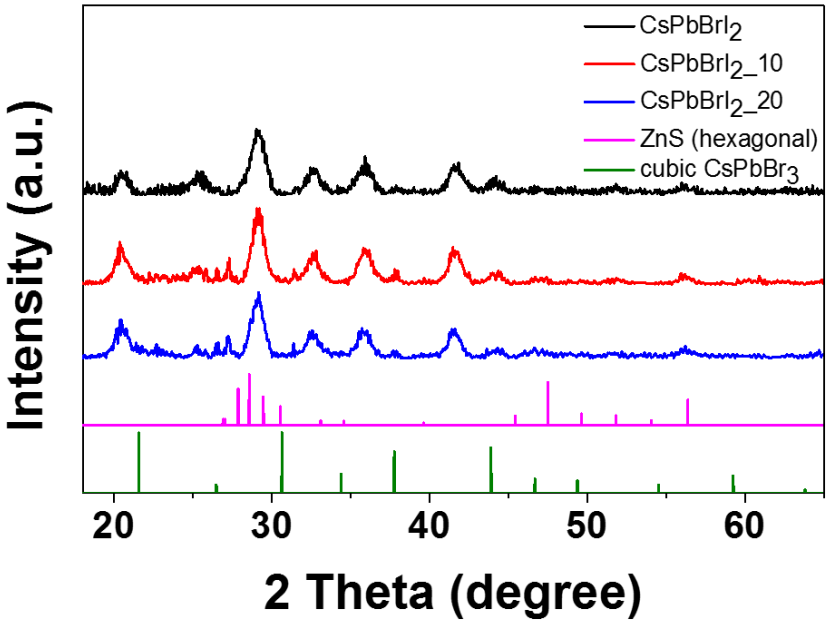

Figure 17. XRD patterns of $CsPbBr_3$/ZnS heterostructures with the amount of precursors.

2.3.4 Stability test of $CsPbX_3$/ZnS heterostructures

One of the disadvantages of perovskite is its instability, which is considered to be the problem for the commercialization of perovskite-based devices. Therefore, I measured the PL wavelengths over time to investigate the improvement of stability for $CsPbBrI_2$/ZnS heterostructures prior to application of organic photovoltaics. The figure 18 shows the stability of PL properties of $CsPbBrI_2$ and $CsPbBrI_2$/ZnS heterostructures under ambient conditions. Pristine $CsPbBrI_2$ was unstable which made the wavelength of PL emission peak shift to 525 nm in less than 2 days. On the other hand, $CsPbBrI_2$/ZnS heterostructures were stable as the amount of Zn and S precursors increased without protection of the air. The PL wavelength of $CsPbBrI_2$/ZnS_10 was shifted from initial 623.8 nm to 564.8 nm by about 59.0 nm after about 18 days. $CsPbBrI_2$/ZnS_20 showed enhanced PL stability by shifting the wavelength from 617.3 nm to 572.5 nm by about 44.8 nm. Due to the oxygen and moisture in the air, the structures of perovskites are weakened, and unstable iodine, one of the constituents of the perovskites structures, escapes, so that the perovskites are decomposed and the PL wavelength is shifted. Therefore, it can be seen that PL stability is improved under ambient condition by forming $CsPbBrI_2$/ZnS heterostructures through these results, and it is further improved as the amount of added Zn and S precursors are increased.

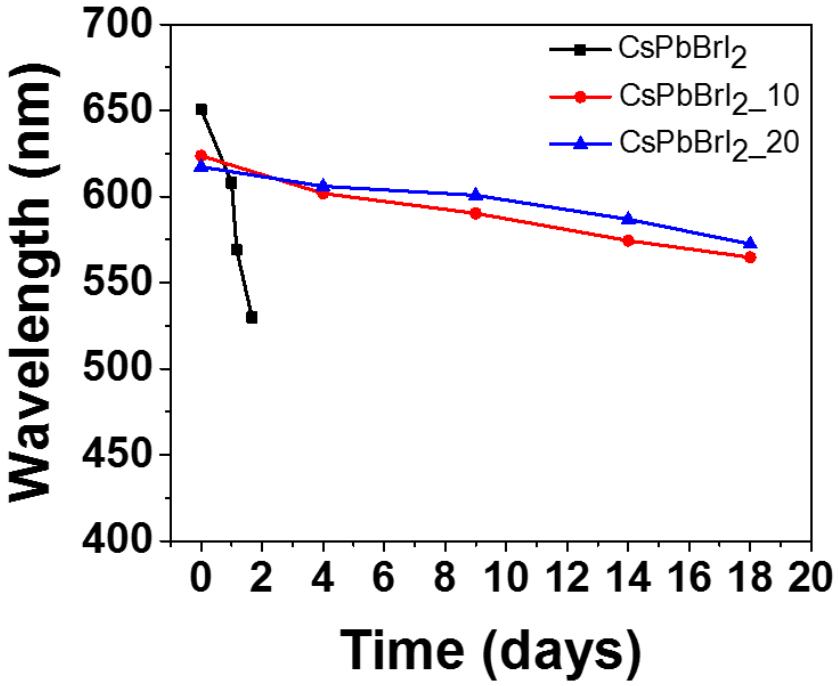

Figure 18. PL emission wavelength over time of $CsPbBr_3$/ZnS heterostructures.

2.3.5 Characterization of organic photovoltaics with $CsPbX_3$/ZnS as additive

The device architecture of the organic photovoltaics (OPVs) with $CsPbX_3$ and $CsPbX_3$/ZnS heterostructures is displayed in Figure 19a. After the ZnO layer was deposited on the ITO substrate as the conventional OPVs structure, $CsPbBrI_2$ was added to the PTB7:$PC_{71}BM$ as an active layer. MoO_3 and Ag were then deposited on them to complete the device cell. The J-V curves of the devices fabricated with various amounts of $CsPbBrI_2$ in active layer, are shown in Figure 19b-c and the corresponding OPVs performances are exhibited in Table 6,7.

First, the power conversion efficiency (PCE) of the reference cell using only PTB7:$PC_{71}BM$ as the active layer is 6.3%. However, when the 5 wt% $CsPbBrI_2$ was added to PTB7:$PC_{71}BM$, the PCE increases significantly to 7.7%. When the concentration of $CsPbBrI_2$ in PTB7:$PC_{71}BM$ was increased to 10 wt%, the efficiency of the resulting device further increased to 8.3%. Further increasing the $CsPbBrI_2$ concentration to 50 wt% resulted in the PCE of the corresponding cell decreasing to 4.1%. Therefore, the PCEs were 8.1% for 7.5 wt% of $CsPbBrI_2$ and 7.8% for 12.5 wt% when I compared the PCEs by the amount around the 10 wt% which was the most efficient. These results were not significantly different from 10 wt%, so the subsequent experiments were carried out with fixed 10 wt% of $CsPbBrI_2$ or $CsPbBrI_2$/ZnS heterostructures.

From these results, it can be seen that PCE of $CsPbBrI_2$ added device is improved more than reference device without $CsPbBrI_2$. GIWAXD analysis was carried out to demonstrate the reason, and the results of the films with or without 10 wt% of $CsPbBrI_2$ were compared (Figure 20). First, the crystallinity of the film with 10 wt% of $CsPbBrI_2$ was improved compared to the reference film without $CsPbBrI_2$. This is because the amorphous peaks of PCBM are weakened and sharp peaks due to crystallinity are strengthened. In both the in-plane and out-of-plane directions, the crystallinity seems to be stronger, but especially the crystallinity of the in-plane is improved.

To identify the effect of stability of OPVs by addition of $CsPbBrI_2$/ZnS heterostructures, I measured the changes in photovoltaic properties of the OPVs with same amount of $CsPbBrI_2$ and $CsPbBrI_2$/ZnS heterostructures as additives for 8 days (Figure 21). As shown in table 8, PCE was increased by adding $CsPbBrI_2$, but the addition of $CsPbBrI_2$/ZnS heterostructures results in a further increase of PCE, leading that $CsPbBrI_2$/ZnS_20 shows a PCE of 7.70%. When $CsPbBrI_2$ was added, the PCE was initially increased to 7.10% but decreased to 5.27% after the 8 days so that the instability of $CsPbBrI_2$ results in not only an increase in initial efficiency but a fast reduction in efficiency. The PCE of reference cell decayed by from 7.08% to 6.51% for 8 days, whereas that of the cell with CsPbBrI2/ZnS_10 as an additive slightly decayed by from 7.62% to 6.70%. $CsPbBrI_2$/ZnS_20 shows the best stability for 8 days and PCE was 7.09% after 8 days which is higher PCE value than reference cell.

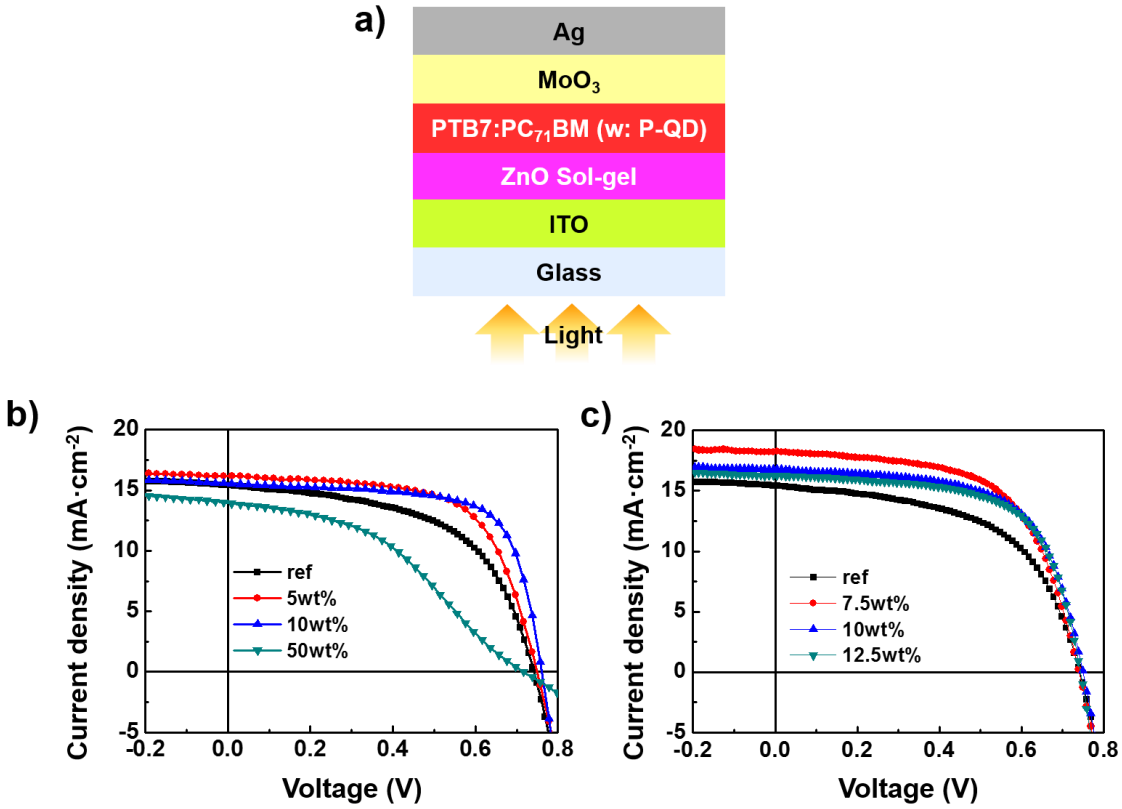

Figure 19. (a) The device architecture of the organic photovoltaics (OPVs), (b,c) J−V curves of OPVs with various amount of $CsPbBrI_2$/ZnS heterostructures as additives.

Table 6. Photovoltaic parameters based on pristine $CsPbBrI_2$ NCs with various amount as additives.

	Jsc ($mA \cdot cm^{-2}$)	**Voc** (V)	**FF** (%)	**PCE** (%)
Ref_PTB7:$PC_{71}BM$	15.4	0.738	55.7	6.3
Ref+$CsPbBrI_2$ (5 wt%)	16.2	0.758	62.9	7.7
Ref+$CsPbBrI_2$ (10 wt%)	15.6	0.758	70.0	8.3
Ref+$CsPbBrI_2$ (50 wt%)	14.0	0.717	40.8	4.1

Table 7. Photovoltaic parameters based on pristine $CsPbBrI_2$ NCs with various amount as additives.

	Jsc ($mA \cdot cm^{-2}$)	**Voc** (V)	**FF** (%)	**PCE** (%)
Ref_PTB7:$PC_{71}BM$	15.4	0.738	55.7	6.3
Ref+$CsPbBrI_2$ (7.5 wt%)	18.2	0.738	60.4	8.1
Ref+$CsPbBrI_2$ (10 wt%)	16.8	0.748	63.0	7.9
Ref+$CsPbBrI_2$ (12.5 wt%)	16.3	0.738	64.6	7.8

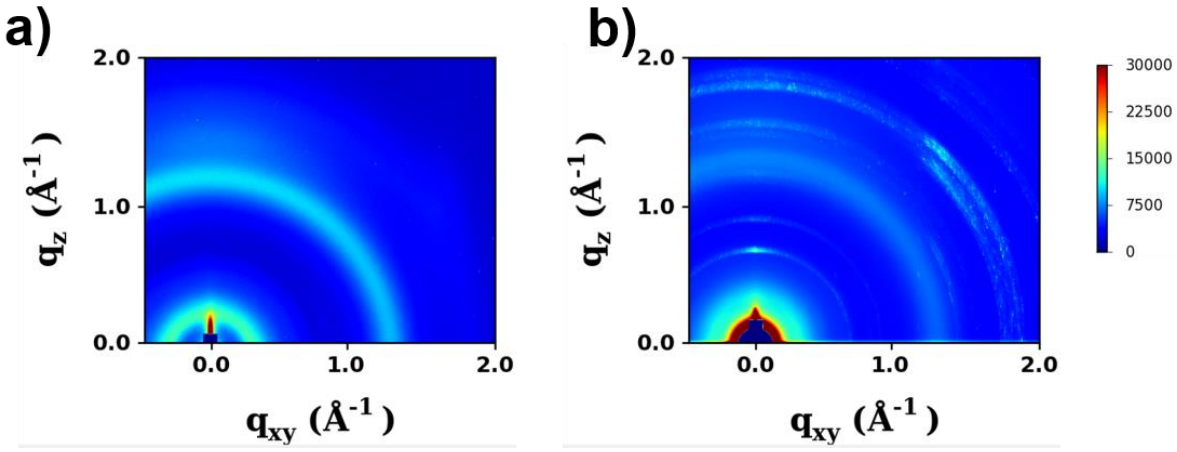

Figure 20. GIWAXD patterns of (a) reference film with only PTB7:$PC_{71}BM$ as active layer, (b) film with $CsPbBrI_2$/ZnS heterostructure added to active layer

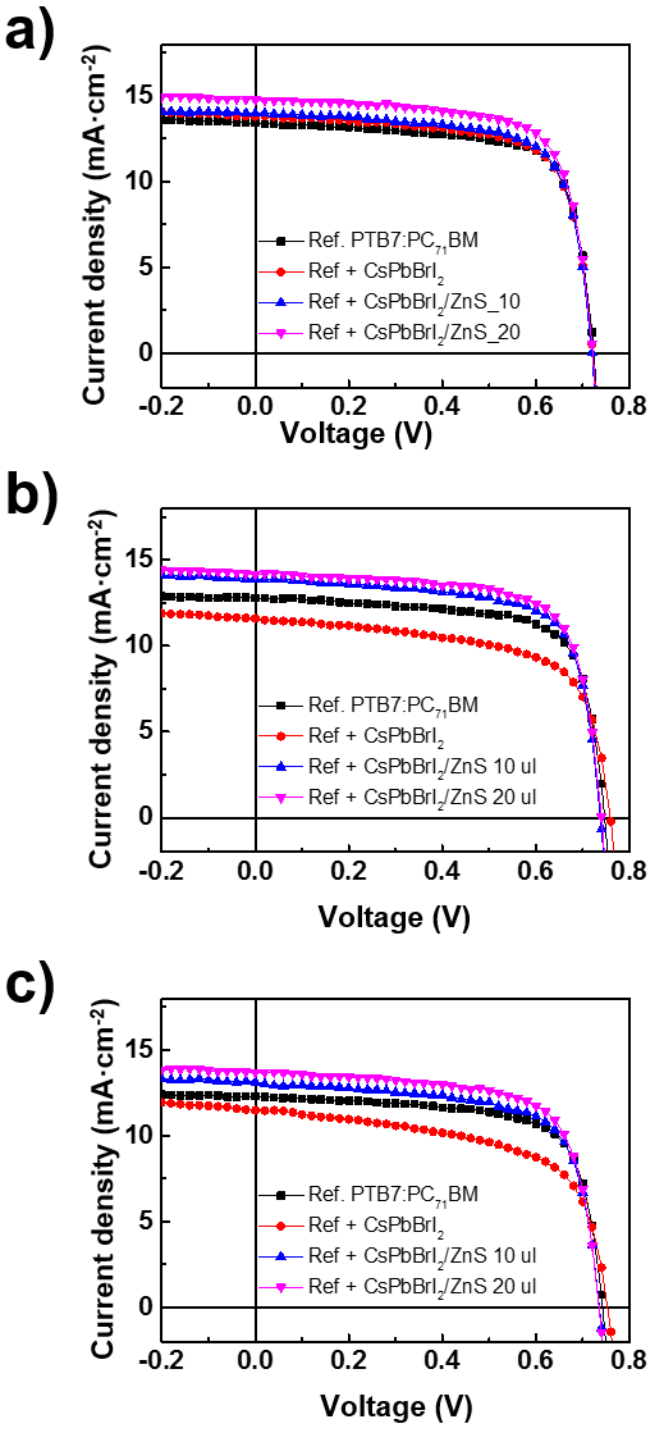

Figure 21. J−V curves of OPVs with various amount of $CsPbBrI_2$/ZnS heterostructures at (a) 0 day, (b) 2 days, (c) 8 days.

Table 8. PCE values of OPVs with various amount of $CsPbBrI_2$/ZnS heterostructures over time.

	0 Day	**2 Days**	**8 Days**
Ref_PTB7:$PC_{71}BM$	7.08	6.83	6.51
Ref+$CsPbBrI_2$	7.10	5.65	5.27
Ref+$CsPbBrI_2$/ZnS_10	7.62	7.29	6.70
Ref+$CsPbBrI_2$/ZnS_20	7.70	7.55	7.09

2.4 Conclusion

In summary, I developed a facile strategy to synthesize $CsPbX_3$/ZnS heterostructures at room temperature to enhance the colloidal stability. The $CsPbX_3$/ZnS heterostructures were synthesized by injecting OAm-Zn^{2+} and DDA-S^{2-} as a ligand-type precursor with high reactivity into purified $CsPbX_3$ NCs, and the optical and structural analysis were carried out. The formation of ZnS on perovskite NCs induces n-type or p-type doping effect, which changes the electronic characteristics. As a result, the emission wavelength of green-emitting $CsPbBr_3$ NCs shifted to longer wavelength and red-emitting $CsPbBrI_2$ NCs were blue-shifted. The formation of $CsPbX_3$/ZnS heterostructures were not influenced by time because of the high reactivity of Zn and S precursors but affected by the amount of precursors. The stability of $CsPbBrI_2$/ZnS heterostructures were determined by measuring the transition of emission wavelength, and the emission peak of pristine $CsPbBrI_2$ NCs was shifted from 525 nm to 625 nm within only 2 days. On the other hand, the emission wavelength of $CsPbBrI_2$/ZnS_10 injected with Zn and S precursors of 10 μl was shifted from 623.8 nm to 564.8 nm by 59.0 nm after 18 days, and $CsPbBrI_2$/ZnS_20 shifted to 572.5 nm by 44.8 nm, indicating the enhanced colloidal stability. In addition, when $CsPbBrI_2$/ZnS heterostructures were applied to organic photovoltaics, they showed improved efficiency due to crystallinity of $CsPbBrI_2$ NCs and stability over 8 days.

Conclusion

The perovskite NCs show exceptional optical and electronic properties, attracting attention as a material for applying to various optoelectronic devices. However, there is a problem that perovskite NCs have very poor stability for commercialization, so that many researchers have studied to enhance the stability of perovskite NCs.

In this work, I synthesized $CsPbX_3$/ZnS heterostructures to improve the colloidal stability and applied it to OPVs to demonstrate improved device stability. $CsPbX_3$/ZnS heterostructures have been reported once in the past, but there are some problems that purification after synthesis is not perfect, and reproduction is not performed well. On the other hand, the facile synthesis method for $CsPbX_3$/ZnS heterostructures in this work is simple, and the purification process is clear, leading to obtain $CsPbX_3$/ZnS heterostructures with high quality. The $CsPbX_3$/ZnS heterostructures were synthesized by injecting OAm-Zn^{2+} and DDA-S^{2-} as a ligand-type precursor with high reactivity into purified $CsPbX_3$ NCs, inducing n-type or p-type doping effect, which changes the electronic characteristics. As a result, I identified the enhanced colloidal stability of $CsPbBrI_2$/ZnS heterostructures by measuring the change of PL emission spectra over time. As the amount of Zn and S precursors increased, the red-emitting $CsPbBrI_2$ NCs were blue-shifted and the stability increased. In addition, when $CsPbBrI_2$/ZnS heterostructures were applied to organic photovoltaics, the maximum PCE was 7.70% compared to reference cell with only PTB7:PC71BM as an active layer. Furthermore, $CsPbBrI_2$/ZnS_20 also showed the PCE of 7.09% even after 8 days, indicating the enhanced device stability.

Therefore, this facile synthesis method for $CsPbX_3$/ZnS heterostructures contributes not only to the stability but also to the improvement of the optical characteristics, so applying to other optoelectronic devices such as LEDs will be effective.

References

1. Weber, D. $CH_3NH_3SnBr_xI_{3-x}$ (X=0-3)-Sn(II)-system with cubic perovskite structure. *Z. Naturforsch. B.* **1978**, 33, 862–865.
2. Mitzi, D. B.; Feild, C. A.; Harrison, W. T. A.; Guloy, A. M. Conducting tin halides with a layered organic-based perovskite structure. *Nature*. **1994**, 369, 467–469.
3. Christians, J. A.; Miranda Herrera, P. A.; Kamat, P. V. Transformation of the excited state and photovoltaic efficiency of $CH_3NH_3PbI_3$ perovskite upon controlled exposure to humidified air. *J. Am. Chem. Soc*. **2015**, 137, 1530–1538.
4. H. Cho,; S.-H. Jeong; M.-H. Park; Y.-H. Kim; C. Wolf, C.-L.; Lee, J. H. Heo; A. Sadhanala, N. Myoung; S. Yoo; S. H. Im; R. H. Friend; T.-W. Lee Overcoming the electroluminescence efficiency limitations of perovskite light-emitting diodes. *Science*. **2015**, 350, 1222-1225
5. Y. Bai; Q. Dong; Y. Shao; Y. Deng; Q. Wang; L. Shen; D. Wang; W. Wei; J. Huang, Enhancing stability and efficiency of perovskite solar cells with crosslinkable silane-functionalized and doped fullerene. *Nature Commun.* **2016**, 7, 12806.
6. Luo, S.; Daoud,W. A. Recent progress in organic-inorganic halide perovskite solar cells: mechanisms and materials design. *J.Mater. Chem. A.* **2015**, 3, 8992.
7. M. Grätzel. The light and shade of perovskite solar cells. *Nat. Mater.* **2014**, 13, 838–842.
8. X. Li, Y. Wu; S. Zhang; B. Cai; Y. Gu; J. Song; H. Zeng. $CsPbX_3$ Quantum Dots for Lighting and Displays: Room-Temperature Synthesis, Photoluminescence Superiorities, Underlying Origins and White Light-Emitting Diodes. *Adv. Funct. Mater*. **2016**, 26, 2435–2445
9. Protesescu, L.; Yakunin, S.; Bodnarchuk, M. I.; Krieg, F.; Caputo, R.; Hendon; C. H., Yang; R. X.; Walsh. A.; Kovalenko. M. V. Nanocrystals of cesium lead halide perovskites ($CsPbX_3$, X=Cl, Br, and I): novel optoelectronic materials showing bright emission with wide color gamut. *Nano Lett.* **2015**, 15, 3692–3696.
10. G. Nedelcu; L. Protesescu; S. Yakunin; M. I. Bodnarchuk; M. J. Grotevent; M. V. Kovalenko. Fast Anion-Exchange in Highly Luminescent Nanocrystals of Cesium Lead Halide Perovskites ($CsPbX_3$, X = Cl, Br, I). *Nano Lett*. **2015**, 15, 5635.
11. Wehrenfennig, C.; Eperon, G. E.; Johnston, M. B.; Snaith, H. J.;Herz, L. M. High Charge Carrier Mobilities and Lifetimes in Organolead Trihalide Perovskites. *Adv. Mater.* **2014**, 26, 1584−1859.
12. D'Innocenzo, V.; Grancini, G.; Alcocer, M. J. P.; Kandada, A. R.S.; Stranks, S. D.; Lee, M. M.; Lanzani, G.; Snaith, H. J.; Petrozza, A. Excitons Versus Free Charges in Organo-Lead Tri-Halide Perovskites. *Nat. Commun*. **2014**, 5, 3586.
13. Stranks, S. D.; Eperon, G. E.; Grancini, G.; Menelaou, C.;Alcocer, M. J. P.; Leijtens, T.; Herz,

L. M.; Petrozza, A.; Snaith, H. J. Electron-Hole Diffusion Lengths Exceeding 1 Micrometer in an Organometal Trihalide Perovskite Absorber. *Science*, **2013**, 342, 341−344.

14. A. Swarnkar; R. Chulliyil, V. K. Ravi; M. Irfanullah, A. Chowdhury; A. Nag; Colloidal $CsPbBr_3$ Perovskite Nanocrystals: Luminescence beyond Traditional Quantum Dots. *Angew. Chem. Int. Ed.* **2015**, 54, 15424 –15428.
15. Wu, K.; Bera, A.; Ma, C.; Du. Y.; Yang, Y.; Li, L.; Wu, T. Temperature-dependent excitonic photoluminescence of hybrid organometal halide perovskite films. *Phys. Chem. Chem. Phys.,* **2014**, 16, 22476–22481.
16. Huang, H.; Bodnarchuk, M.; Kershaw, S. V.; Kovalenko, M. V.; Rogach, A. L. Lead Halide Perovskite Nanocrystals in the Research Spotlight: Stability and Defect Tolerance *ACS Energy Lett.* **2017**, 2, 2071−2083.
17. A. Kojima.; K. Teshima.; Y. Shirai.; T. Miyasaka.; *J. Am. Chem. Soc.,* **2009**, 131, 6050–6051.
18. NREL, Best Research-Cell Efficiencies, http://www.nrel.gov,accessed: November 2017.
19. G. E. Eperon.; G. M. Paterno.; R. J. Sutton.; A. Zampetti.; A. A. Haghighirad.; F. Cacialli.; H. J. Snaith. *J. Mater. Chem. A*. **2015**, 3, 19688
20. A. Swarnkar.; A. R. Marshall.; E. M. Sanehira.; B. D. Chernomordik.; D. T. Moore.; J. A. Christians.; T. Chakrabarti.; J. M. Luther.; *Science.* **2016**, 354, 92-95.
21. Zhang, W.; Eperon, G. E.; Snaith, H. J. Metal halide perovskites for energy applications. *Nat. Energy*. **2016**, 1, 16048-16056
22. J. Song.; J. Li.; X. Li.; L. Xu.; Y. Dong.; H. Zeng. Quantum Dot Light-Emitting Diodes Based on Inorganic Perovskite Cesium Lead Halides ($CsPbX_3$). *Adv. Mater*. **2015**, 27, 7162-7167.
23. Chiba, T.; Hoshi, K.; Pu, Y.-J.; Takeda, Y.; Hayashi, Y.; Ohisa, S.; Kawata, S.; Kido, J. High-Efficiency Perovskite Quantum-Dot Light-Emitting Devices by Effective Washing Process and Interfacial Energy Level Alignment. *ACS Appl. Mater. Interfaces*. **2017**, 9, 18054–18060.
24. Zhang, X.; Sun, C.; Zhang, Y.; Wu, H.; Ji, C.; Chuai, Y.; Wang, P.; Wen, S.; Zhang, C.; Yu, W. W. Bright Perovskite Nanocrystal Films for Efficient Light-Emitting Devices. *J. Phys. Chem. Lett.* **2016**, 7, 4602–4610.
25. Pan, J.; Quan, L. N.; Zhao, Y.; Peng, W.; Murali, B.; Sarmah, S. P.; Yuan, M.; Sinatra, L.; Alyami, N. M.; Liu, J.; Yassitepe, E.; Yang, Z.; Voznyy, O.; Comin, R.; Hedhili, M. N.; Mohammed, O. F.; Lu, Z. H.; Kim, D. H.; Sargent, E. H.; Bakr, O. M. Highly Efficient Perovskite-Quantum-Dot Light-Emitting Diodes by Surface Engineering. *Adv. Mater.* **2016**, 28, 8718–8725.
26. M.V. Kovalenko.; L. Protesescu.; M.I. Bodnarchuk. Properties and potential optoelectronic applications of lead halide perovskite nanocrystals. *Science.* **2017**, 358, 745–750
27. T. Leijtens.; B. Lauber.; G. E. Eperon.; S. D. The Importance of Perovskite Pore Filling in

Organometal Mixed Halide Sensitized TiO_2-Based Solar Cells. *J. Phys. Chem. Lett.* **2014**, 5, 1096−1102

28. Guarnera, S.; Abate, A.; Zhang, W.; Foster, J. M.; Richardson, G.; Petrozza, A.; Snaith, H. J. Improving the Long-Term Stability of Perovskite Solar Cells with a Porous Al_2O_3 Buffer Layer. *J. Phys. Chem. Lett*. **2015**, 6, 432−437
29. Dirin, D. N.; Protesescu, L.; Trummer, D.; Kochetygov, I. V.; Yakunin, S.; Krumeich, F.; Stadie, N. P.; Kovalenko, M. V Harnessing Defect-Tolerance at the Nanoscale: Highly Luminescent Lead Halide Perovskite Nanocrystals in Mesoporous Silica Matrixes. *Nano Lett*. **2016**, 16, 5866−5874
30. JY Sun.; FT Rabouw.; XF Yang.; XY Huang.; XP Jing.; Shi Ye.; QY Zhang. Facile Two-Step Synthesis of All-Inorganic Perovskite $CsPbX_3$ (X = Cl, Br, and I) Zeolite-Y Composite Phosphors for Potential Backlight Display Application. *Adv. Funct. Mater*. **2017**, 1704371-1704371
31. Yi, W.; Xiaoran, D.; Zhongxi, X.; Xuechao, C.; Sisi, L.; Ping'an, M.; Zhiyao, H.; Ziyong, C.; Enhancing the Stability of Perovskite Quantum Dots by Encapsulation in Crosslinked Polystyrene Beads via a Swelling–Shrinking Strategy toward Superior Water Resistance. *Adv. Funct. Mater.* **2017**, 27, 1703535-1703535
32. Meyns, M.; Peralvarez, M.; Heuer-Jungemann, A.; Hertog, W.; Ibanez, M.; Nafria, R.; Genc, A.; Arbiol, J.; Kovalenko, M. V.; Carreras, J.; Cabot, A.; Kanaras, A. G. Polymer-Enhanced Stability of Inorganic Perovskite Nanocrystals and Their Application in Color Conversion LEDs. *ACS Appl. Mater. Interfaces.* **2016**, 8, 19579−19586
33. Wang, C.; Chesman, A. S.; Jasieniak, J. J. Stabilizing the cubic perovskite phase of $CsPbI_3$ nanocrystals by using an alkyl phosphinic acid. *Chem. Commun.* **2017**, 53, 232-235
34. Pan, J.; Sarmah, S. P.; Murali, B.; Dursun, I.; Peng, W.; Parida, M. R.; Liu, J.; Sinatra, L.; Alyami, N.; Zhao, C.; et al. Air-Stable Surface-Passivated Perovskite Quantum Dots for Ultra-Robust, Single- and Two-Photon-Induced Amplified Spontaneous Emission. *J. Phys. Chem. Lett.* **2015**, 6, 5027−5033
35. Woo, J. Y.; Kim, Y.; Bae, J.; Kim, T. G.; Kim, J. W.; Lee, D. C.; Jeong, S. Highly Stable Cesium Lead Halide Perovskite Nanocrystals through in Situ Lead Halide Inorganic Passivation. *Chem. Mater.* **2017**, 29, 7088−7092
36. Hines, M. A.; Guyot-Sionnest, P. Synthesis and Characterization of Strongly Luminescing ZnS-Capped CdSe Nanocrystals. *J. Phys. Chem.* **1996**, 100, 468.
37. Chen, W.; Hao, J.; Hu, W.; Zang, Z.; Tang, X.; Fang, L.; Niu, T.; Zhou, M. Enhanced Stability and Tunable Photoluminescence in Perovskite $CsPbX_3$/ZnS Quantum Dot Heterostructure. *Small*. **2017**, 13, 1604085

38. Jiang, P.; Zhu, C.-N.; Zhu, D.-L.; Zhang, Z.-L.; Zhang, G.-J.; Pang, D.-W. A room-temperature method for coating a ZnS shell on semiconductor quantum dots. *J. Mater. Chem. C*, **2015**, 3, 964–967
39. T. Torimoto.; T. Adachi.; K. Okazaki.; M. Sakuraoka.; T. Shibayama.; B. Ohtani.; A. Kudo.; S. Kuwabata. Facile Synthesis of ZnS-$AgInS_2$ Solid Solution Nanoparticles for a Color-Adjustable Luminophore. *J. Am. Chem. Soc.* **2007**, 129, 12388
40. L. Yi.; Y. Liu.; N. Yang.; Z. Tang.; H. Zhao.; G. Ma.; Z. Su.; D. Wang. One dimensional CuInS2–ZnS heterostructured nanomaterials as low-cost and high-performance counter electrodes of dye-sensitized solar cells. *Energy Environ. Sci*. **2013**, 6, 835-840
41. N. Soltani.; E. Saion.; M. Z. Hussein.; M. Erfani.; A. Abedini.; G. Bahmanrokh.; M. Navasery.; P. Vaziri. Visible Light-Induced Degradation of Methylene Blue in the Presence of Photocatalytic ZnS and CdS Nanoparticles. *Int. J. Mol. Sci*. **2012**, 13, 12242-12258